NAVAL POSTGRADUATE SCHOOL
Monterey, California

AD-A243 896

91-17182

THESIS

TWO NONLINEAR MODELS
OF THE
FREE ELECTRON LASER

by

David H. Kiel

December, 1990

Thesis Advisor: William B. Colson

91 12

REPORT DOCUMENTATION PAGE		Form Approved OMB No 0704-0188

1a REPORT SECURITY CLASSIFICATION UNCLASSIFIED	1b RESTRICTIVE MARKINGS
2a SECURITY CLASSIFICATION AUTHORITY Multiple Sources	3 DISTRIBUTION/AVAILABILITY OF REPORT Unlimited Distribution
2b DECLASSIFICATION/DOWNGRADING SCHEDULE	

4 PERFORMING ORGANIZATION REPORT NUMBER(S)	5 MONITORING ORGANIZATION REPORT NUMBER(S)

6a NAME OF PERFORMING ORGANIZATION Naval Postgraduate School	6b OFFICE SYMBOL (If applicable) 33	7a NAME OF MONITORING ORGANIZATION Naval Postgraduate School
6c ADDRESS (City, State, and ZIP Code) Monterey, Ca 93940,5000		7b ADDRESS (City, State, and ZIP Code) Monterey Ca, 93940,5000

8a NAME OF FUNDING/SPONSORING ORGANIZATION	8b OFFICE SYMBOL (If applicable)	9 PROCUREMENT INSTRUMENT IDENTIFICATION NUMBER
8c ADDRESS (City, State, and ZIP Code)		10 SOURCE OF FUNDING NUMBERS

	PROGRAM ELEMENT NO	PROJECT NO	TASK NO	WORK UNIT ACCESSION NO

11 TITLE (Include Security Classification)

TWO NONLINEAR MODELS OF THE FREE ELECTRON LASER

12 PERSONAL AUTHOR(S)
Kiel, David H.

13a TYPE OF REPORT Masters Thesis	13b TIME COVERED FROM _____ TO _____	14 DATE OF REPORT (Year, Month, Day) Dec 1990	15 PAGE COUNT 73

16 SUPPLEMENTARY NOTATION The views expressed in theis thesis are those of the author and do not reflect the official policy or position of the Department of Defense or the U.S. Govt.

17 COSATI CODES			18 SUBJECT TERMS (Continue on reverse if necessary and identify by block number)
FIELD	GROUP	SUB-GROUP	FEL, Macroparticle, Oscillator,

19 ABSTRACT (Continue on reverse if necessary and identify by block number)

The dynamics of the Free Electron Laser are governed by Maxwell's equations which causes many highly nonlinear regimes to exist in Free Electron Laser Physics. This thesis will examine two such areas and develop simple models to describe the highly dynamic and rich behavior two of these regimes.

In the strong-field, high-current regime, the Free Electron Laser driving current can be modeled by a single macroparticle representing the trapped electrons. When the trapped electrons act collectively as a macroparticle, solutions which include synchrotron oscilations can be found for the self-consistent pendulum and wave equations.

In as FEL Oscillator with low single-pass gain, the evolution of the optical wave can lead to sideband development. This phenomenon is studied by applying Maxwell's equations to an oscillator with two optical modes and

20 DISTRIBUTION/AVAILABILITY OF ABSTRACT [X] UNCLASSIFIED/UNLIMITED ☐ SAME AS RPT ☐ DTIC USERS	21 ABSTRACT SECURITY CLASSIFICATION Unclassified	
22a NAME OF RESPONSIBLE INDIVIDUAL W.B. Colson	22b TELEPHONE (Include Area Code) (408) 646-2116	22c OFFICE SYMBOL 61CW

DD Form 1473, JUN 86   Previous editions are obsolete   SECURITY CLASSIFICATION OF THIS PAGE

S/N 0102-LF-014-6603   Unclassified

deriving a two-mode wave and pendulum equation. The two-moke wave and pendulum equations are implemented numerically on computers so that the onset of the sideband can be explored.

Approved for public release; distribution is unlimited.

Two Nonlinear Models

of the

Free Electron Laser

by

David H. Kiel

Lieutenant, United States Navy

B.A., University of Colorado

Submitted in partial fulfillment

of the requirements for the degree of

MASTER OF SCIENCE IN PHYSICS

from the

NAVAL POSTGRADUATE SCHOOL

December 1990

Author: _____

David H. Kiel

Approved by: _____

William B. Colson, Thesis Advisor

_____

Andres Larraza, Second Reader

_____

Karlheinz E. Woehler, Chairman

Department of Physics

iii

ABSTRACT

The dynamics of the Free Electron Laser are governed by Maxwell's equations which causes many highly nonlinear regimes to exist in Free Electron Laser Physics. This thesis will examine two such areas and develop simple models to describe the highly dynamic and rich behavior two of these regimes.

In the strong-field, high-current regime, the Free Electron Laser driving current can be modeled by a single macroparticle representing the trapped electrons. When the trapped electrons act collectively as a macroparticle, solutions which include synchrotron oscillations can be found for the self-consistent pendulum and wave equations.

In an FEL oscillator with low single-pass gain, the evolution of the optical wave can lead to sideband development. This phenomenon is studied by applying Maxwell's equations to an oscillator with two optical modes and deriving a two-mode wave and pendulum equation. The two-mode wave and pendulum equations are implemented numerically on computers so that the onset of the sideband can be explored.

TABLE OF CONTENTS

ACKNOWLEDGEMENTS

To my loving wife and children who demonstrated much patient and understanding during the final weeks of writing this thesis.

I INTRODUCTION

Free Electron Lasers (FELs) are proving to be an exciting and practical source of radiation with a wide assortment of applications over a broad range of the RF spectrum. First proposed in 1970 by John Madey [Ref.1], and experimentally demonstrated by Madey and his colleagues in 1975 and 1976 [Ref. 2,3], they are now being considered for use in a wide variety of applications. The FEL is based on the original work by Motz who demonstrated that light could be amplified by an electron beam propagating through a periodic magnetic field [Ref. 4,5,6]. In 1960, the ubitron was developed by Phillips which operates on similar principals to the FEL [Ref. 7].

The FEL has many attributes that make it attractive for a wide assortment of uses. The most notable of these attributes is the FEL's continuous tunability. FELs have been demonstrated to operate over a range of frequencies that varied by a factor of 10 [Ref. 8]. Closely related to continuous tunability is the "designability" of the FEL. The same basic theory and mechanisms that work for a FEL operating in the millimeter range will also work in the tens of nanometer range. FELs can also be scaled to high power applications since the gain medium contains only a relativistic electron beam in a periodic magnetic field, and does not suffer the nonlinear material affects that plague convention atomic lasers in the high power regimes. This also makes FELs very reliable since the weakest link in FEL design, the accelerator, is generally considered very reliable. FELs do suffer two major drawbacks, size and cost. Some of the current work in FELs is aimed at reducing the size which will help with the associated high cost [Ref. 8].

Another active area of FEL research is in the high-power regime where they have many applications ranging from plasma heating to weaponry. Unfortunately, in the high-power regimes,

two different areas where nonlinearities arise, and develop simple theories that provide useful insight into these dynamic regimes.

Chapter II will provide the necessary background on classical FEL theory. Chapter III will develop a simple theory that treats the bunched electrons in the FEL as a single macroparticle. This greatly simplifies the FEL dynamics and allows simple solutions to be derived describing FEL behavior in this highly nonlinear regime. The solutions can then be used to study the trapped-particle instability, sideband development, and chaos in the FEL. The solutions can also be used for design criteria. Chapter IV develops a simple two-mode model of the FEL oscillator by solving Maxwell's equations for two optical modes in the oscillator. The model is then used to study the growth of sidebands in an oscillator. A quantitative understanding of this phenomenon will add a tremendous degree of control in FEL oscillator design.

II FREE ELECTRON LASER THEORY

A. BASIC FREE ELECTRON LASER PHYSICS

An FEL consists of two major components, an electron accelerator to produce a relativistic electron beam and a wiggler or undulator with a static, periodic magnetic field to "wiggle" the electrons with a periodic oscillatory motion. It is this periodic motion of the electrons in the undulator that causes radiation in the forward direction. Some of this spontaneous radiation is saved in the laser resonator causing stimulated emission that leads to coherent radiation. Since the electron beam is highly relativistic, the electrons "see" the undulator's magnetic field wavelength as being much shorter due to relativistic Lorentz contraction. Subsequently, the optical field produced by the *undulating electrons is of a much shorter wavelength than the undulator's magnetic field wavelength.*

The above is a Quantum Mechanical description of the basic FEL physics. Despite this, the FEL mechanism is essentially classical and can be adequately described with Electro-Magnetic Theory. Figure 2-1, illustrates the major features of the classical approach.

The incoming electrons enter the undulator and begin to oscillate due to the periodic magnetic *field of the undulator as shown in the top of Figure 2-1.* The oscillating action of the electrons causes them to emit photons in a manner analogous to a radiating antenna. In the middle of Figure 2-1, one undulator wave section is enlarged to show both the optical and magnetic fields of the undulator superimposed over the oscillating path of the electron. The forces acting on the electrons are governed by the Lorentz force law

$$\frac{d(\gamma\vec{\beta})}{dt} = -\frac{e}{mc}(\vec{E} + \vec{\beta} \times \vec{B}) \quad , \quad \dot{\gamma} = -\frac{e}{mc}(\vec{\beta}\cdot\vec{E}) \quad , \qquad 2\text{-}1$$

where $\vec{\beta} = \vec{v}/c$ and $\gamma^{-2} = 1 - \beta^2$. The speed of light is c, the mass of the electron is m, the electron charge is e, and the velocity of the electron is $\vec{v}$. $\vec{E}$ and $\vec{B}$ represent the electric and magnetic fields present in the undulator from both the optical wave and the static undulator magnetic field. By
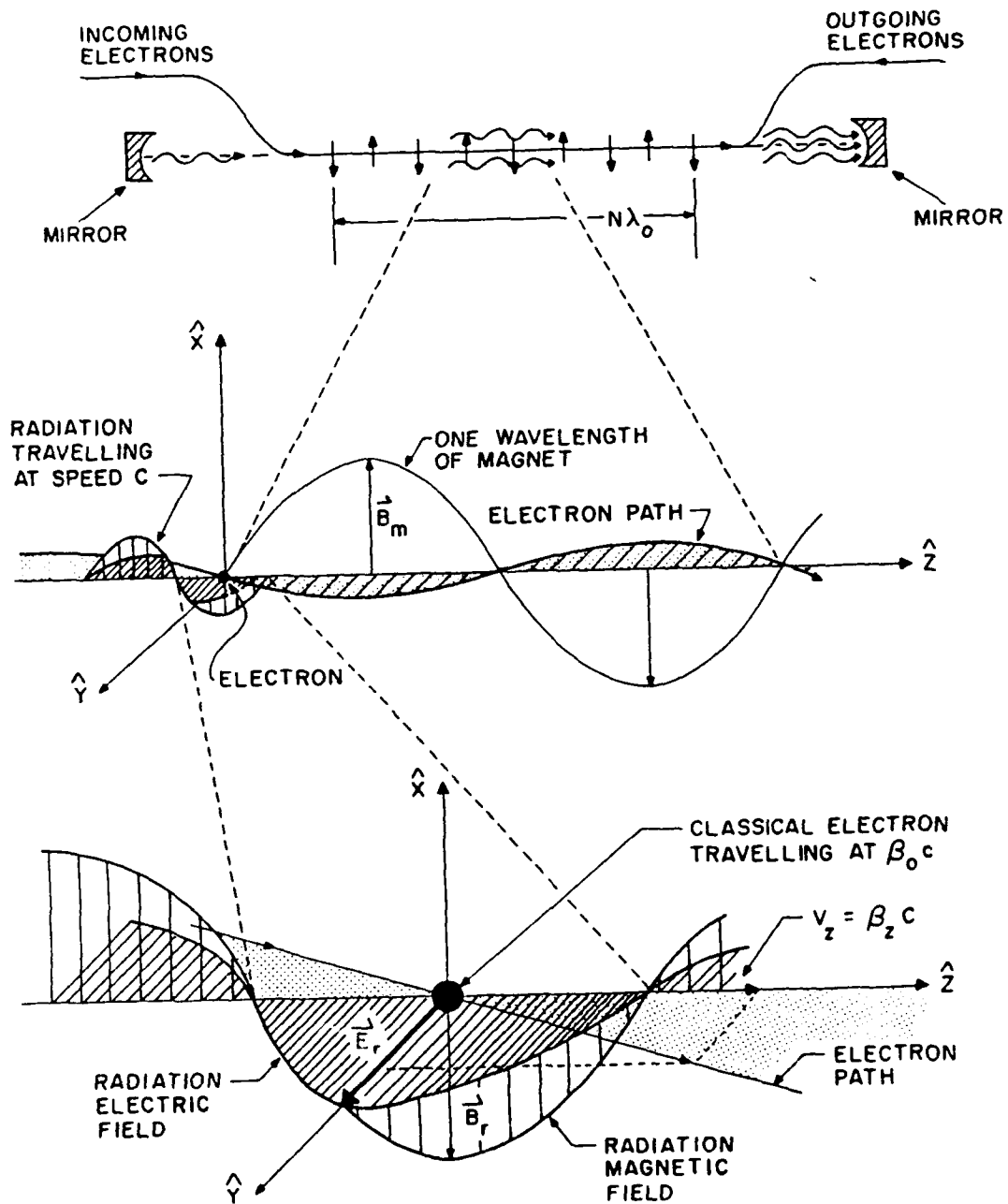
3

Figure 2-1: Major components of the Free Electron Laser illustrating the fundamental physics of the laser.

4

examining the bottom third picture in Figure 2-1, it can be seen that the electrons are effected by the optical field and the effect is dependent on the electron's phase relative to the optical field. This coupling between the electrons and the optical wave is best illustrated with an example. When the electron has a velocity component both in the z direction and out of the page, and the magnetic field of the optical wave is directed downward, the electron will experience a force retarding its forward motion and causing the electron to lose energy. Conservation of energy requires that the electron's lost energy go to the optical wave causing subsequent amplification of the optical field. Different electron phases with respect to the optical field can also cause the electron to gain energy from the optical field. Therefore, careful analysis is required of the electron and optical field coupling to produce amplification of the optical field.

B.   ELECTRON DYNAMICS AND THE PENDULUM EQUATION

In order to fully understand the interaction of the electrons and the optical field inside the undulator, the equations governing the evolution of the electrons must be developed. Begin by assuming a *helically polarized static magnetic undulator field of the form*:

$$\vec{B} = B(\cos(k_0 z),\ \sin(k_0 z),\ 0)\ ,$$

2-2

where B is the field strength, z is the distance along the longitudinal axis of the undulator, and k_0 is the wave number of the undulator's magnetic field. Also assume that a circularly polarized plane wave is present in the undulator cavity of the form

$$\vec{E}_R = E(\cos\psi,\ -\sin\psi, 0),\qquad \vec{B}_R = E(\sin\psi,\ \cos\psi, 0)\ ,$$

2-3

where E is the optical field strength and $\psi = kz - \omega t + \phi$ with $\omega = kc$. The wave number for the optical field is denoted by k, time by t, and the optical phase by ϕ.

5

Substituting equations 2-2 and 2-3 into the Lorentz force equations, 2-1, and separating the electron motion into their transverse and longitudinal components the following is obtained

$$\frac{d(\gamma \vec{\beta}_\perp)}{dt} = -\frac{e}{mc}[E(1-\beta_z)(\cos\psi,-\sin\psi,0)+\beta_z B(-\sin k_0 z,\cos k_0 z,0)] \quad , \qquad 2\text{-}4$$

$$\frac{d(\gamma \beta_z)}{dt} = -\frac{e}{mc}[E(\beta_x\cos\psi - \beta_y\sin\psi) + B(\beta_x\sin k_0 z - \beta_y\cos k_0 z)] \quad , \qquad 2\text{-}5$$

and

$$\frac{d\gamma}{dt} = -\frac{e}{mc}E[\beta_x\cos\psi-\beta_y\sin\psi] \quad , \qquad 2\text{-}6$$

where $\vec{\beta}_\perp = (\beta_x,\beta_y,0)$. Since the electrons are highly relativistic, the approximation $1-\beta_z \approx 0$ can be used to show that $E(1 - \beta_z) \ll B\beta_z$ [Ref. 8]. This simplifies the transverse equation 2-4 and allows it to be solved by inspection giving

$$\vec{\beta}_\perp = -\frac{K}{\gamma}(\cos k_0 z,\sin k_0 z,0) \quad , \qquad 2\text{-}7$$

where $K = eB\lambda_o/2\pi mc^2$ is a dimensionless parameter that characterizes the properties of the undulator. In a FEL K is usually close to 1. The transverse motion solution, 2-7, assumes perfect beam injection so that there are no constants of integration. The transverse motion is on a much smaller scale than the average z motion along the z axis [Ref. 8].

Substituting the transverse motion, 2-7, into equation 2-6 gives

$$\dot{\gamma} = -\frac{eKE}{mc\gamma}(\cos(k_0 z)\cos\psi - \sin(k_0 z)\sin\psi) \quad . \qquad 2\text{-}8$$

Using trigonometric identity for the cosine of the sum of two angles and the definition

6

$\zeta \equiv (k + k_0)z - \omega t$ the change of the electron's energy is found to be

$$\dot{\gamma} = \frac{eKE}{\gamma mc}\cos(\zeta + \phi) \quad .$$

2-9

ζ is a dimensionless "microscopic" variable that describes the electron's phase with respect to the optical wave and the undulators magnetic field. ζ is on the "scale" of λ, the wavelength of the optical wave in the undulator, since $k \gg k_0$ and $z \approx ct$. The exchange of energy of the electrons is easily understood in terms of the electron's phase from 2-9. For example, electrons with phases such that, $-\pi/2 \leq (\zeta + \phi) \leq \pi/2$, will receive energy from the optical wave causing them to accelerate. Other electrons at phases, $\pi/2 \leq (\zeta + \phi) \leq 3\pi/2$ will lose energy to the optical wave. Since some electrons gain and some electrons lose energy, a beam of initially random, but essentially continuously spaced electrons, will begin to bunch during the trip down the undulator. This bunching process is the important feature of the FEL gain mechanism as will be discussed in more detail in section D.

To further simplify the dynamics of the electrons in the undulator, it is convenient to relate $\dot{\gamma}$ to $\ddot{\zeta}$. Using the definition

$$\gamma^{-2} \equiv 1 - \beta^2 = 1 - \beta_z^2 - \beta_\perp^2 \quad ,$$

2-10

and recalling 2-7, for the $\beta_\perp$ motion, we have

$$\gamma^{-2} = 1 - \beta_z^2 - \frac{K^2}{\gamma^2} \quad ,$$

2-11

since $\beta_\perp^2 = K^2/\gamma^2$. Solving equation 2-11 for β_z and differentiating with respect to time gives

$$\dot{\beta}_z = \frac{(1 + K^2)}{\gamma^2} \frac{\dot{\gamma}}{\gamma} \quad ,$$

2-12

using $\gamma \gg 1$, and $\beta_z \approx$. Differentiating the definition of ζ twice respect to time, and solving for $\dot{\beta}_z$ gives

7

$$\dot{\beta}_z = \frac{\zeta}{(k + k_o)c} \quad . \qquad \text{2-13}$$

Equating 2-11 and 2-12 gives

$$\frac{\dot{\gamma}}{\gamma} = \frac{\zeta}{(k + k_o)c} \frac{\gamma^2}{1 + K^2} \quad . \qquad \text{2-14}$$

When one wavelength of light passes over an electron as the electron traverses one undulator wavelength, the electron is in resonance with the optical wave, and the electron is oscillating at the same rate as the optical field so that $\zeta = 0$. Using this, the resonance condition can be derived which will be used to simplify 2-14. Starting with the definition of ζ and differentiating with respect to time yields

$$\dot{\zeta} = (k + k_0)c\beta_z - kc = 0 \quad . \qquad \text{2-15}$$

Solving 2-11 for β_z and substituting into 2-15 yields

$$\frac{\lambda_o}{2\lambda} = \frac{\gamma^2}{(1 + K^2)} \quad , \qquad \text{2-16}$$

since $\gamma \gg 1$.

Combining equations 2-14 and 2-16 and solving for $\dot{\gamma}$ gives

$$\dot{\gamma} = \frac{\zeta\gamma}{(k + k_o)c} \frac{\lambda_o}{2\lambda} = \frac{\zeta\gamma}{(k + k_o)c} \frac{k}{2k_0} \quad . \qquad \text{2-17}$$

Since $k \gg k_o$,

$$\dot{\gamma} \approx \frac{\gamma\zeta}{2k_o c} = \frac{\gamma\zeta}{2\omega_o} \qquad \text{2-18}$$

Equating equation 2-9, the energy equation, and equation 2-18, and solving for ζ gives

8

$$\ddot{\zeta} = \frac{2e\omega_o KE}{\gamma^2 mc} \cos(\zeta + \phi) \qquad \text{2-19}$$

which is the simple pendulum equation. To put the pendulum equation, 2-19, in dimensionless form, define a dimensionless time $\tau = ct/L$, such that $0 \leq \tau \leq 1$, where L is the length of the undulator. Applying the chain rule gives $d^2\zeta/d\tau^2 = \ddot{\zeta}(L/c)^2$ so that

$$\overset{\circ\circ}{\zeta} = \frac{2e\omega_o KEL^2}{\gamma^2 mc^3} \cos(\zeta + \phi) = \frac{4\pi eKELN}{\gamma^2 mc^2} \cos(\zeta + \phi) \ , \qquad \text{2-20}$$

since $k_o c = \omega_o = c2\pi/\lambda_o$. N is the number of periods in the magnetic field of the undulator and the " $\circ$ " refers to differentiation with respect to τ , as will always be the case. Defining $|a| \equiv (4\pi eKELN)/(\gamma^2 mc^2)$ as the dimensionless optical field strength so that the optical field is $a = |a|e^{i\phi}$ gives

$$\overset{\circ\circ}{\zeta} = |a| \cos(\zeta + \phi) \ . \qquad \text{2-21}$$

The pendulum equation given in equation 2-21 is valid for both strong and weak-fields. The only restrictions placed on using equation 2-21 are that γ be high enough that the electron is not bent excessively by the undulator's magnetic field and that the FEL is not so efficient that γ decreases substantially as the electron traverse the undulator. The optical field strength $|a|$ in front of the cos term explains why stronger optical fields produce rapid electron evolution.

As the FEL normally saturates, the electrons lose enough energy that they drop out of the gain bandwidth. As the electrons continue to lose energy and shift across the gain bandwidth, the beam's phase velocity $v = \overset{\circ}{\zeta}$ decreases by $\Delta v \approx 4\pi N\Delta\gamma/\gamma \approx -2\pi$. By either decreasing the undulator's magnetic field wavelength λ_o along the z axis, or by decreasing the magnetic field strength B along z, or both, the electrons could be accelerated in phase-space to maintain resonance with the optical wave. Each method is conceptually equivalent and both are called "tapering" the undulator [Ref. 8]. The phase acceleration can be added to the pendulum equation as an added constant that is turned on near saturation at time τ_s. This makes the pendulum equation

9

$$\zeta \atop = \begin{cases} |a| \cos(\zeta + \phi) & \tau < \tau_s \\ \delta + |a| \cos(\zeta + \phi) & \tau > \tau_s \end{cases} \qquad \text{2-22}$$

where δ is the necessary added phase acceleration. When the phase acceleration is created by decreasing the undulators wavelength, $\delta \sim -2\pi N \Delta\lambda_o/\lambda_o$ and when the acceleration is provided by weakening the magnetic field $\delta \sim -4\pi N K^2 \Delta B/B(1+K^2)$ [Ref. 8]. If $\delta > |a|$, then the path of the electron in phase-space will not repeat itself nor return to its initial conditions. Paths in phase-pace that do not repeat themselves are called open orbits. Paths that do close on themselves and repeat are called closed orbits. If $|a| > \delta$ some of the electrons can be trapped in closed orbits, and with $|a| \gg \delta$ most of the electrons can be trapped near resonance around $\zeta \approx \pi$ producing high gain. Successful tapering requires strong optical fields [Ref. 8].

C.   OPTICAL WAVE EVOLUTION AND THE WAVE EQUATION

In both FEL oscillators and FEL amplifiers, spontaneous emission rapidly forms a classical wave with some degree of coherence since the bandwidth of the spontaneously emitted light is comparable to the inverse of the number of undulator periods traversed by the electrons [Ref. 8]. As discussed during the pendulum equation's derivation, there is either energy loss or gain depending on the electron's phase relative to the optical wave.

The optical wave is taken to vary slowly in time during an optical period ($\dot{E} \ll \omega E$, $\dot{\phi} \ll \omega\phi$) and vary slowly in space over an optical wavelength ($E' \ll kE$, $\phi' \ll k\phi$) . This approximation is known as the slowly varying amplitude and phase approximation (SVAP) and is consistent with the narrow bandwidth expected for any laser. The evolving optical wave can be viewed as a carrier wave made up of a single high frequency that is modulated by a complex wave envelope that varies slowly in amplitude and phase over many optical wavelengths. It is this complex envelope that meets the SVAP approximation. If the complex wave envelope did not meet the SVAP approximation, the light from the laser would have a much broader bandwidth than expected and poor coherence. This is evident through Fourier analysis.

To begin the derivation of the FEL wave equation, assume a circularly polarized plane-wave

10

is established in the undulator as in 2-3 of the previous section with a vector potential of the form

$$\vec{A} = \frac{E_R(t)}{k}(\sin\psi, \cos\psi, 0) \quad , \qquad\qquad 2\text{-}23$$

where all the variables are the same as those defined in 2-3. Using the vector potential in the wave equation [Ref. 8]

$$\left(\vec{\nabla}^2 - \frac{1}{c^2}\frac{\partial^2}{\partial t^2}\right)\vec{A} = -\frac{4\pi}{c}\vec{J}_t \quad , \qquad\qquad 2\text{-}24$$

where $\vec{J}_T$ is the transverse current from the transverse motion of the electron beam, and the SVAP approximation to eliminate all terms with two derivatives, gives

$$\left(\vec{\nabla}^2 - \frac{1}{c^2}\frac{\partial^2}{\partial t^2}\right)\vec{A} \approx \frac{2}{c}\frac{\partial E_R}{\partial t}(\cos\psi, -\sin\psi, 0) -$$

$$\frac{2E_R}{c}\frac{\partial\phi}{\partial t}(\sin\psi, \cos\psi, 0) = -\frac{4\pi}{c}\vec{J}_t \quad . \qquad\qquad 2\text{-}25$$

The sin and cos functions of ψ in equation 2-25 rotate fast with respect to the slowly evolving complex envelope. To eliminate this fast rotation in equation 2-25, two orthogonal unit vectors can be defined,

$$\hat{\varepsilon}_1 \equiv (\cos\psi, -\sin\psi, 0) \quad , \qquad \hat{\varepsilon}_2 \equiv (\sin\psi, \cos\psi, 0) \quad , \qquad\qquad 2\text{-}26$$

to project into 2-25. This reduces Maxwell's second-order vector equation, 2-25, into two first-order scaler equations

$$\hat{\varepsilon}_1 \cdot \left(\vec{\nabla}^2 - \frac{1}{c^2}\frac{\partial^2}{\partial t^2}\right)\vec{A} \approx \frac{2}{c}\frac{\partial E_R}{\partial t} = -\frac{4\pi}{c}\vec{J}_t \cdot \hat{\varepsilon}_1 \qquad\qquad 2\text{-}27$$

11

and

$$\hat{e}_2 \cdot \left(\vec{\nabla}^2 - \frac{1}{c^2} \frac{\partial^2}{\partial t^2} \right) \vec{A} \approx \frac{2E_R}{c} \frac{\partial \phi}{\partial t} = -\frac{4\pi}{c} \vec{J}_t \cdot \hat{e}_2 \quad . \qquad 2\text{-}28$$

The single-particle current is given by $\vec{J}_t = -ec\vec{\beta}\delta^3(\vec{x} - \vec{r}_i)$ where $\vec{r}_i$ is the position of the i'th electron, and $\delta^3(\vec{x} - \vec{r}_i)$ is a three dimensional Dirac delta function [Ref. 9]. This implies that the transverse single-particle current with the transverse motion $\beta_\perp$ from 2-7 of the previous section is

$$\vec{J}_{\perp t} = \frac{e^2 B}{\gamma m \omega_o} (\cos(k_o z), \sin(k_o z), 0) \, \delta^3(\vec{x} - \vec{r}_i) \quad , \qquad 2\text{-}29$$

where B is the field strength of the undulator's magnetic field, m is the electron mass and ω_0 is the radial frequency of the undulator's magnetic field. Substituting the single-particle transverse current, 2-29, into the first-order Maxwell equations, 2-27 and 2-28, and taking the appropriate dot products gives

$$\vec{J}_t \cdot \hat{e}_1 = \frac{e^2 B}{\gamma m \omega_o} \cos(\psi + k_o z) \delta^3(\vec{x} - r_i) \quad . \qquad 2\text{-}30$$

and

$$\vec{J}_t \cdot \hat{e}_2 = \frac{e^2 B}{\gamma m \omega_o} \sin(\psi + k_o z) \delta^3(\vec{x} - r_i) \quad . \qquad 2\text{-}31$$

Summing over all the particles to obtain the total transverse current and averaging both equations at a fixed time over a volume element dv that is much smaller than the coherence volume but much larger than the optical wavelength, gives [Ref. 8]

12

$$\frac{1}{c}\frac{\partial E_R}{\partial t} = -\frac{2\pi eK}{\gamma}\rho \langle \cos(\zeta + \phi) \rangle \ , \qquad\qquad 2\text{-}32$$

and

$$E_R\left(\frac{1}{c}\frac{\partial \phi}{\partial t}\right) = -\frac{2\pi eK}{\gamma}\rho \langle \sin(\zeta + \phi) \rangle \ , \qquad\qquad 2\text{-}33$$

where ρ is the particle density and the brackets represent the ensemble average over all the electrons. Equations 2-32 and 2-33 can be simplified further by introducing another dimensionless parameter

$$j = \frac{8N(e\pi KL)^2\rho}{\gamma^3 mc^2} \ , \qquad\qquad 2\text{-}34$$

representing the dimensionless current of the electron beam [Ref. 8]. The dimensionless current, j, along with the dimensionless field strength $|a|$ simplifies equation 2-32 and 2-33 to

$$|\overset{\circ}{a}| = -j\langle \cos(\zeta + \phi) \rangle \ , \qquad\qquad 2\text{-}35$$

and

$$\overset{\circ}{\phi} = \frac{j}{|a|}\langle \sin(\zeta + \phi) \rangle \ . \qquad\qquad 2\text{-}36$$

The above two equations describe how the complex optical field evolves with the electron beam. With high-current densities, $j > \pi$, the gain will be high since $|\overset{\circ}{a}|$ will be large. Also, strong optical fields will slow down the evolution of the optical phase. The above wave equation used with the pendulum equation of section B describe the simple FEL optical and electron evolution. In general, the pendulum and wave equations have no simple analytical solution, but are easy to simulate numerically to show the major features of FEL physics. Section E will present numerical simulations that demonstrate important FEL physics.

13

D. FREE ELECTRON LASER GAIN

1. Low-Current, Weak-Field Gain

In weak-fields and low-current, an approximate solution to the pendulum equation, 2-21, can be obtained by assuming that ϕ and $|a|$ are constant. Using conservation of energy in the undulator and relating Δv, from the pendulum equation's solution, to the change of energy in the optical field, an analytic equation can be found to give the gain of the FEL for weak-fields and low-current [Ref. 8].

The derivation begins by finding a second-order perturbation solution to the pendulum equation assuming weak-fields and low-current so that $\dot{\phi} \approx 0$ and $|\dot{a}| \approx 0$. The solution is

$$\zeta(\tau) = \zeta_0 + v_0\tau - \frac{|a_0|}{v_0^2}\left[\cos(\zeta_0 + v_0\tau) - \cos(\zeta_0) + v_0\tau\sin(\zeta_0)\right]+... \quad , \qquad 2\text{-}37$$

so that

$$v(\tau) = v_0 + \frac{|a_0|}{v_0}\left[\sin(\zeta_0 + v_0\tau) - \sin(\zeta_0)\right] +$$

$$\frac{a_0^2}{v_0^3}\left[-\frac{1}{4}(\cos(2\zeta_0 + 2v_0\tau) - \cos(2\zeta_0)) + \cos(v_0\tau) - \qquad\qquad 2\text{-}38\right.$$

$$\left. 1 - v_0\tau\sin(\zeta_0)\cos(\zeta_0 + v_0\tau)\right]+... \quad .$$

At injection, the electrons form an essential continuum that are evenly spread in phase space. As the electrons evolve along the orbits in phase-space some will gain energy and move ahead in phase space while others will lose energy and fall behind. This bunching occurs on the scale of an optical wavelength. Since the optical wave evolves slowly in time and space, each adjacent 2π section of phase-space is essentially the same as its neighbors over many optical wave lengths allowing equation 2-38 to be spatially averaged over a single 2π length giving

14

$$\langle v \rangle = \frac{1}{2\pi} \int_0^{2\pi} d\zeta_0 = \frac{|a_0|^2}{v_0^3} \left[\cos(v_0 \tau) - 1 + \frac{1}{2} v_0 \tau \sin(v_0 \tau) \right] . \qquad 2\text{-}39$$

From the resonance condition, it can be shown that $\Delta v = 4\pi N \Delta \gamma / \gamma$ [Ref. 8]. Therefore, the change of energy in the optical wave can be found from the average change of energy of the electron beam due to conservation of energy. Namely,

$$dP = \frac{-(\rho F dV) \gamma mc^2 (\langle v \rangle - v_0)}{4\pi N} , \qquad 2\text{-}40$$

where ρ is the real current density, F is the ratio of the "effective" cross-sectional area of the electron beam over the optical beam and is known as the filling factor, and dV is a microscopic volume element one optical wavelength long and with the thickness of the optical beam.

The optical power in a similar microscopic volume with a length of one optical wavelength and cross sectional area of the optical beam is $P = 2E^2 dV / 8\pi$. Therefore, since gain is defined as $G \equiv dP/P$, the gain is

$$G = \frac{-\rho F dV [\gamma mc^2 (\langle v \rangle - v_0)/4\pi N]}{[2E^2 dv/8\pi]} . \qquad 2\text{-}41$$

Substituting equation 2-39 for $\langle v \rangle$ and the dimensionless current density defined in 2-34 into 2-41 gives

$$G(v_0) = \frac{j[2 - 2\cos(v_0 \tau) - v_0 \tau \sin(v_0 \tau)]}{v_0^3} \qquad 2\text{-}42$$

Figure 2-2 is a plot of the low-gain curve. It is interesting to note that the optimal gain occurs at $v_o \approx 2.6$ rather than on-resonance or far off-resonance. This is because near resonance, the electrons can not drop a large distance through phase-space. Far above resonance, $v_o \gg \pi$ the gain will oscillate many times along the undulator resulting in small final gain. In this low-current, weak-field regime, gain is not exponential.

15

```
**** Gain and Phase Curves ****
j=1            a₀=1            σ=0
               N=100          δζ=0
```
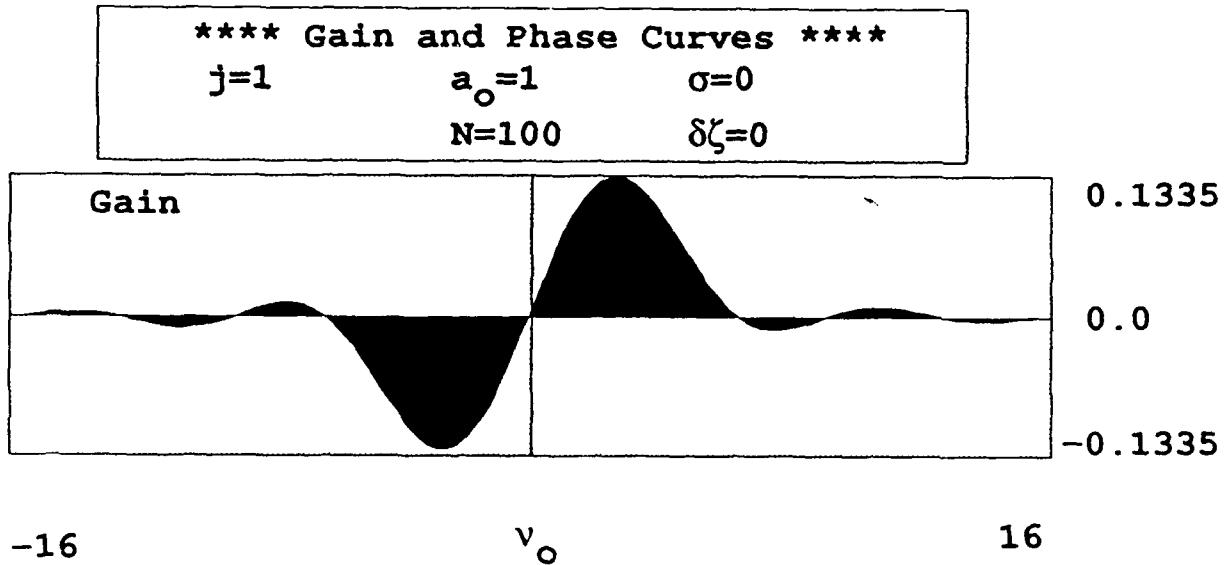
Figure 2-2: The weak field gain spectrum for low current.

2. High-Current, Strong-Field Gain

A gain spectrum, $G(a_0, v_0)$, is easily obtained numerically by calculating the gain at the end of a simulation at each point (v_0, a_0) with current j . Figure 2-3 is the result of such a calculation.

For weak-fields $|a_0| \leq \pi$ the profile in Figure 2-3 is essentially that derived analytically in section 1 and plotted in Figure 2-2; ie it is anti-symmetric with a peak gain of $G = 0.135j$ at $v_0 = 2.6$. However, as the initial field strength increases, the peak gain of Figure 2-3 shifts to higher v_0 . This is due to the large initial separatrix, whose height is $2\sqrt{|a|}$, that can now trap more particles farther off-resonance. The trapped electrons can then lose more energy dropping through phase-space. Also, the peak gain diminishes with higher field strengths. This is saturation,
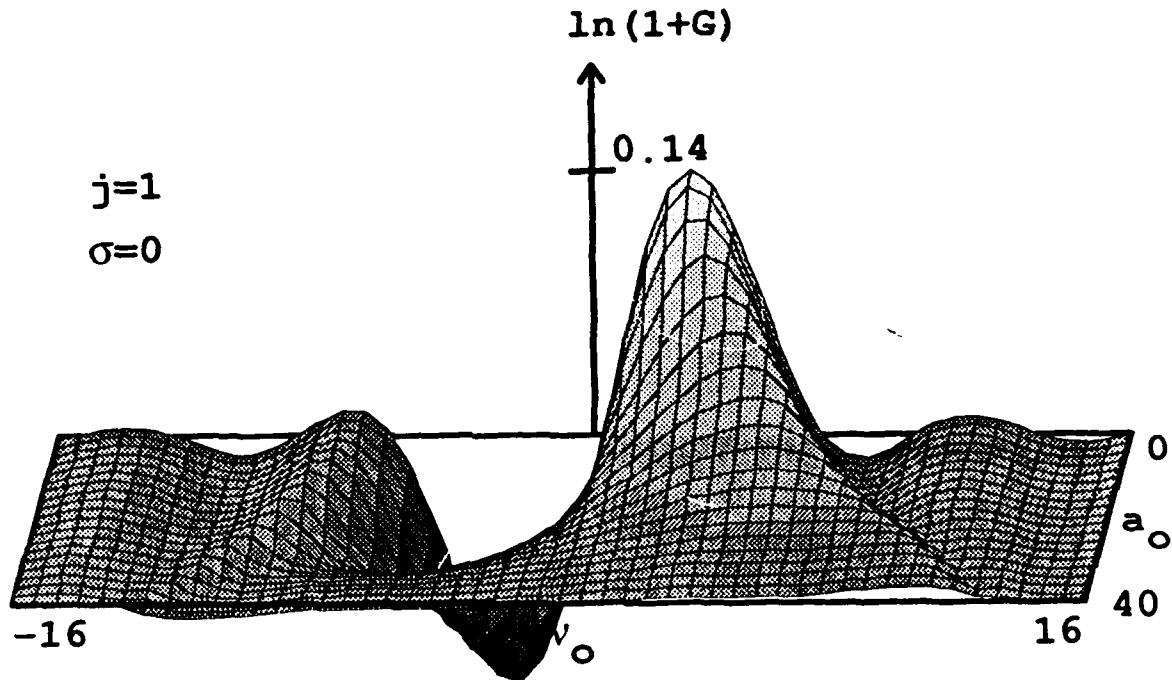
16

Figure 2-3. The gain spectrum for high current with increasing initial field strength.

and is caused by the trapped particles in the closed orbits of phase-space. After trapping, the particles "slosh" back and forth in phase-space producing synchrotron oscillations as will be described in detail later in section E.4. Finally, note that the gain spectrum distorts and the gain bandwidth broadens in ν_0 [Ref. 8].

3. Gain Degradation Due to Beam Quality

Free Electron Laser design often involves a trade off between high-current and beam quality from the accelerator. Since the optical wavelength is usually set by the application, the dimensionless current j is determined by either the real current or the number of undulator periods. Increasing the real current degrades beam quality by producing a beam with more energy spread which degrades the maximum theoretical gain. Conversely, increasing the number of undulator periods to increase

coupling, may decrease the maximum theoretical gain since the undulator is now more sensitive to angular spread of the beam.

Emittance is the measure of the electron beam quality, and is a constant given by the product of the average radial and angular spread of the electrons $\varepsilon_y = \bar{y}\bar{\theta}_y$. It can be shown [Ref. 8] that the average decrease of phase velocity due to the emittance of the beam is

$$\Delta\bar{v}_\beta \approx -\frac{2\pi N}{1+K^2}(K^2 k_o^2 y_0^2 + \gamma^2\theta_y^2) \quad . \qquad \text{2-43}$$

In order to get an understanding how the spread of phase-velocities affects gain, it is necessary to assume weak-fields and combine the wave and pendulum equations. First, solve the pendulum equation for the i'th electron with a first-order perturbation $\zeta_i \approx \zeta_{oi} + v_i\tau + \zeta^{(1)}$, and substitute this solution into the wave equation. Integrating over all initial phase velocities, $\int dv_o$, gives an integro-differential equation governing the evolution of the optical field

$$\overset{\circ}{a}(\tau) = \frac{ij}{2}\int_0^\tau d\tau'\,\tau'F(\tau')e^{-iv_o\tau'}a(\tau-\tau') \quad , \qquad \text{2-44}$$

where $F(\tau') = \int dq\,f(q)e^{-iq\tau'}$ is the characteristic function for the distribution $f(q)$, and $f(q)$ is the initial distribution of electron phase velocities $v_i = v_o+q$ about v_o . In the integral equation, 2-44, all reference to electron phases has been removed, but there still exists the average distribution of initial electron phase velocities [Ref. 8].

Two common distributions exist, the Gaussian

$$f_G(q) = \frac{\exp(-q/2\sigma_G^2)}{\sqrt{2\pi}\,\sigma_G} \quad , \qquad \text{2-45}$$

and the exponential

$$f_\theta(q) = \frac{\exp(q/\sigma_\theta)}{\sigma_\theta} \qquad \text{for } q<0 \quad . \qquad \text{2-46}$$

18

These common distributions have an easy functional form, but real beams generally have additional factors complicating their shape and their exact functional form is unknown. Still the Gaussian and exponential forms provide realistic insight to the gain degradation problem which can be explored by substituting one of their functional forms into the integral equation 2-44 and integrating it numerically
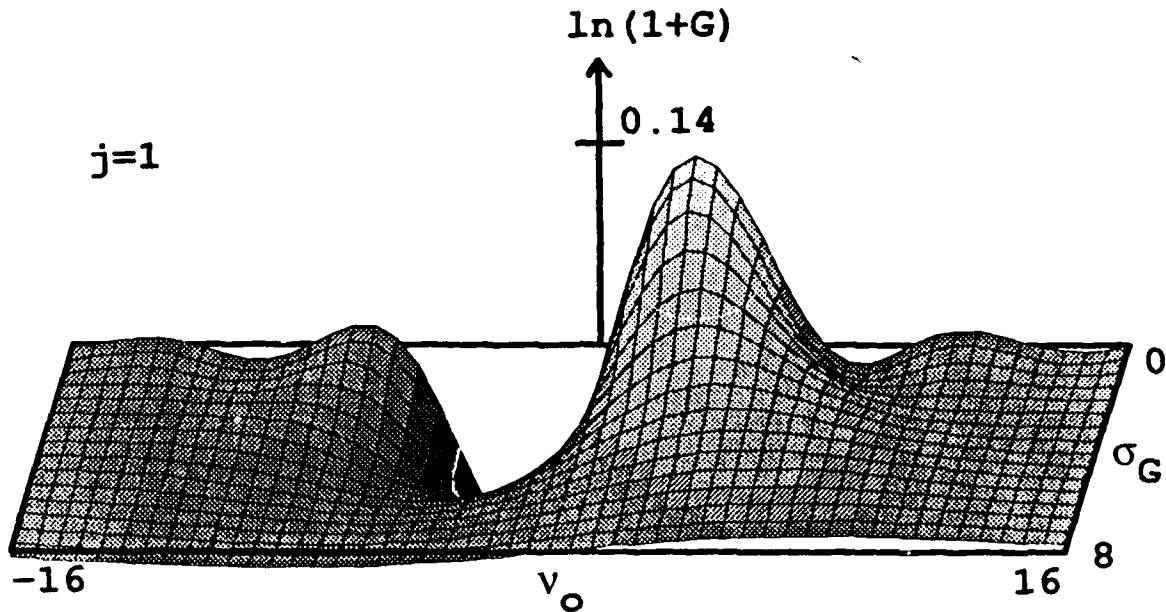

Figure 2-4: The weak field gain profile for low current with an increasing Gaussian energy spread.

to obtain the gain profile in Figure 2-4. Several features are immediately evident from Figure 2-4. First, the peak gain decreases steadily as the beam quality decreases with bigger σ . The peak gain also shifts further off-resonance with poorer beam quality and finally, the gain bandwidth becomes wider. These general features are common to many other beam distributions, but the details of the degradation can be dramatically different. With high-currents, $j \gg 1$, and poor beam quality, the gain is exceeding difficult to predict and can be off by several orders of magnitude [Ref. 8].

4. High-Current, Weak-Field Gain

In the high-current, weak-field regime, the integral equation, 2-44, can be used to develop analytic solutions for the optical field strength and phase. In order to solve the integral equation, consider an FEL with perfect beam quality, $f(\tau') = 1$, and starting on-resonance, $v_0 = 0$. Taking successive derivatives of 2-44 then gives, $\overset{\infty}{a} = ija(\tau)/2$, which has a general solution involving three roots of the form $a_n \exp(\alpha_n \tau)$. The coefficients are determined by the initial conditions $a(0) = a_0$ and $\overset{o}{a}(0) = \overset{\infty}{a}(0) = 0$. The exponents α_n are complex roots of the cubic equation $\alpha_n^3 - ij/2 = 0$ giving a solution which is the sum of all three roots

$$a(\tau) = \frac{a_0}{3}\left[\exp(j/2)^{1/3}(i + \sqrt{3})\tau/2 + \exp(j/2)^{1/3}(i-\sqrt{3})\tau/2 + \exp{-i(j/2)^{1/3}\tau}\right] . \qquad 2\text{-}47$$

During the bunching process, $\tau < \tau_B \approx (2/j)^{1/3} \ll 1$, 2-47 reduces to

$$a(\tau) = a_0(1 + ij\tau^3/12 +...) , \qquad\qquad 2\text{-}48$$

implying that the optical field strength remains esser...ₐₗ𝑦 constant while the phase increases proportional to τ^3. With high-currents only the fastest growing root dominates after the bunch is complete giving

$$|a(\tau)| \approx \frac{a_0}{3}\exp(j/2)^{1/3}\sqrt{3}\ \tau/2 , \qquad \phi(\tau) \approx (j/2)^{1/3}\tau/2 , \qquad 2\text{-}49$$

implying that the gain is exponential until the onset of strong-fields. With large currents, $j \gg 1$, the optical phase shift is large as well.

E. NUMERICAL SIMULATION OF FREE ELECTRON LASER DYNAMICS

The pendulum and wave equations, 2-22, 2-35 and 2-36 are three nonlinear differential equations that have no easy, general analytic solution. However, they are easy to implement numerically and can be used to illustrate major features of FEL physics.

20

1. Electron Bunching

Figure 2-5, illustrates electron bunching with a monoenergetic, low-current beam with a weak optical field present. The electrons are at resonance, $v_0 = \zeta_0 = 0$. The large plot in Figure 2-5 shows the evolution of the electrons in phase-space. The phase-space plot is a plot of the electron's phase, ζ, versus the electron's phase-velocity and reveals many of the FEL's dynamics. The initial positions of the electrons are shown in light grey and become darker as they evolve. The separatrix separates orbits that repeat and close on themselves, closed-orbits, from open-orbits that do not close on themselves. The separatrix shifts position with time due to the ϕ term in the pendulum equation. The separatrix is plotted in this simulation as the black line in phase-space. It can be shown [Ref. 8] that the separatrix height is $2|a|^{1/2}$. The remaining two smaller plots show
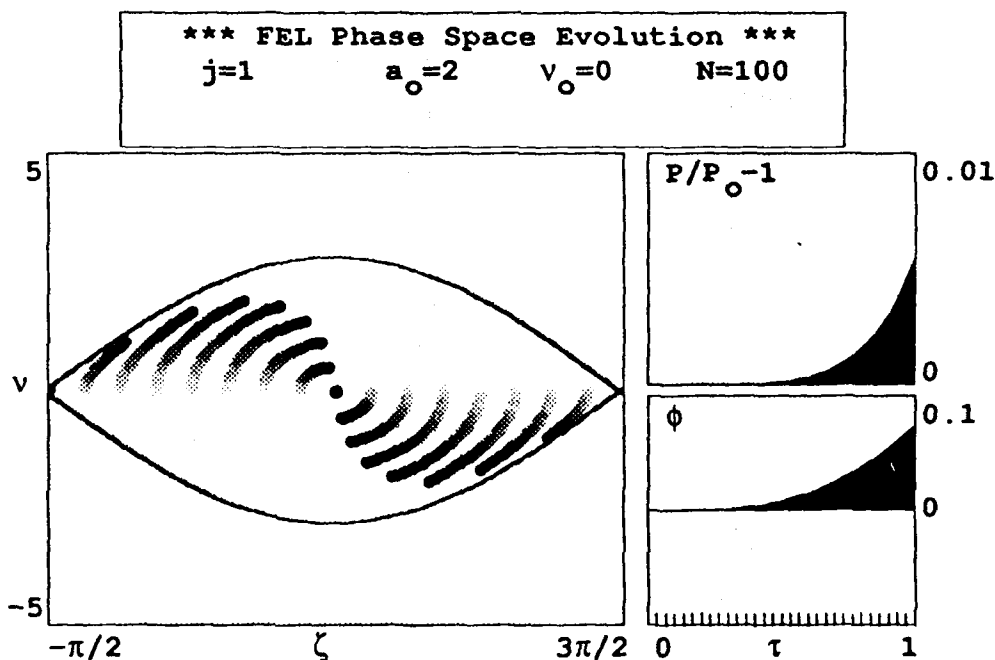

*** FEL Phase Space Evolution ***

$j=1 \qquad a_0=2 \qquad v_0=0 \qquad N=100$

Figure 2-5: Electron bunching with sample electrons on resonance.

21

gain and the evolution of the optical wave's phase ϕ . At time $\tau = 0$ the electrons enter the undulator evenly spaced in phase with respect to the optical wave, and begin travelling down the undulator slightly slower than the optical wave. The electrons whose phase $\pi/2 < \zeta + \phi \leq 3\pi/2$ lose energy and begin to fall back in phase space while those electrons with $-\pi/2 < \zeta + \phi < \pi/2$ gain energy and accelerate in phase space. This bunching, under the right conditions, can trap particles in the separatrix and leads to substantial gain and subsequent saturation as will be demonstrated in section E.3. In this example, the gain is minimal since approximately half the electrons gained and half lost energy. The little gain that exists is due to the optical phase shift, ϕ , that causes the separatrix to shift slightly from its initial position leaving the average position of the electrons slightly greater than $\pi/2$.

2. Low-Currents

To achieve non-trivial gain, it is best to start the electrons off-resonance as illustrated Figure 2-6. Here the electrons were started at $v = 2.6$ and $a_0 = 2$ with a low-current and weak initial fields. More electrons were used to show the virtual continuum of electrons present in the undulator as well as increase the accuracy of the simulation. Note that the most dense bunching occurs near $\zeta \approx \pi$ where the phase space paths are directed downward implying the highest loss of energy for the electrons, and henceforth the largest gain. Also, note that the electrons followed the open orbits outside the separatrix, and that there was only a minimal shift in the optical phase.

3. Strong-Fields, Low-Currents, and Saturation

Figure 2-7 shows a simulation that demonstrates saturation in a low-current, but strong-field FEL as might occur during a single pass in a FEL oscillator. In this simulation the electron beam is no longer monoenergetic, but has a Gaussian distribution of phase-velocities with a width of $\sigma_g = 5$. This more realistic situation prevents all the particles from being trapped inside separatrix, which ultimately lowers the maximum theoretical gain that would have been obtained with a monoenergetic beam as discussed in section D.1 and D.3. The dots in phase space represent the final positions of the electrons at the end of the simulation rather than their time evolution through
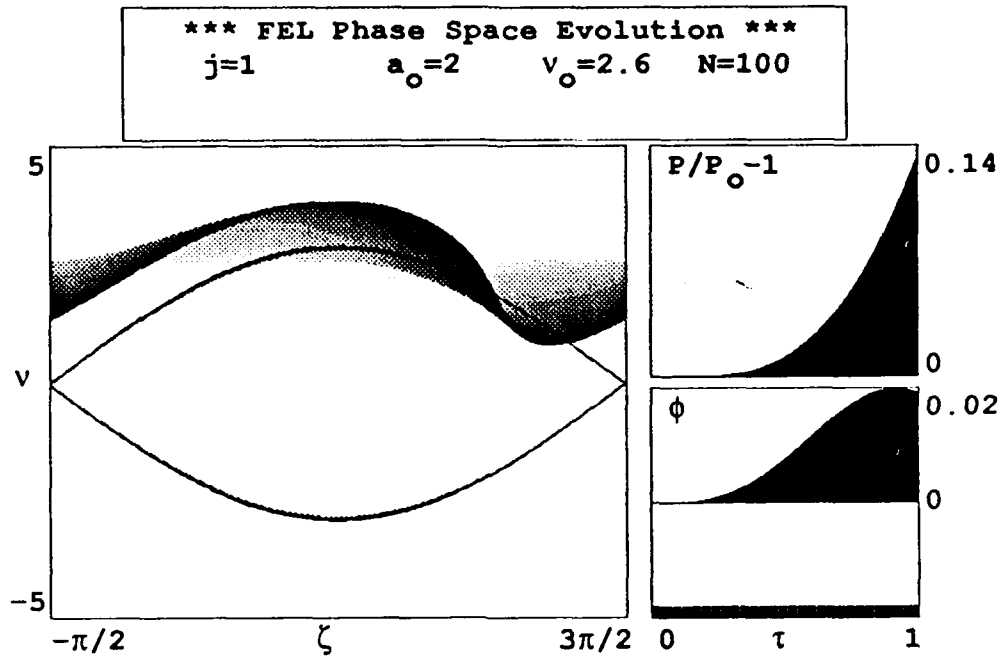
22

Figure 2-6: *Starting electrons off resonance increases gain for a single pass through the undulator.*

phase-space. The electron dynamics of this simulation illustrate several important FEL features. Due to the initial energy spread in the beam, many of the electrons did not become trapped inside the separatrix and are more spread out in phase-space than those that are bunched inside the separatrix. Inside the separatrix, the electrons bunch quickly due to the strong-fields and the optical power grows exponentially as the electron bunch moves past $\zeta + \phi \approx \pi$ at about $\tau \approx 1/2$. It is the peak to peak height of the separatrix, $4 |a|^{1/2}$, at this point that determines the amount of energy that the electrons can transfer to the wave since $\Delta v(\tau) \approx 4 |a|^{1/2}$. This change of phase velocity is enough to move the electron bunch across the gain bandwidth. The growth begins to slow down until near $\zeta + \phi \approx \pi/2$ where the electrons lost all the energy possible, and flow into the $-\pi/2 < \zeta + \phi < \pi/2$ region of phase space where the electrons will take energy from the optical wave and cause the drop in gain.
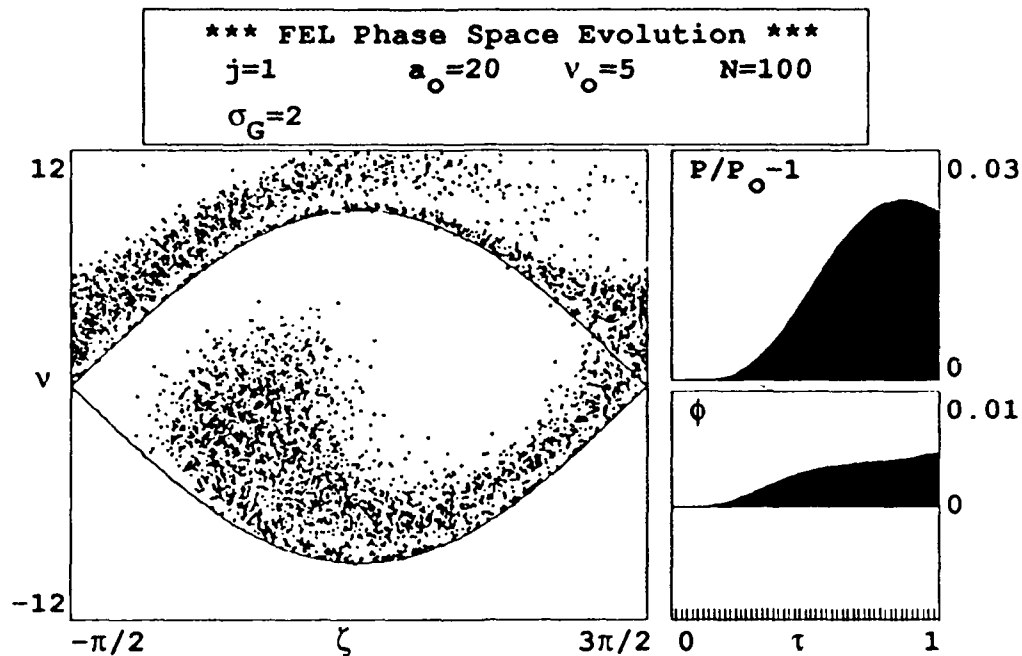
23

*** FEL Phase Space Evolution ***

j=1 a_0=20 v_0=5   N=100

σ_G=2

12

P/P_0-1   0.03

0

v

ϕ 0.01

0

-12

-π/2 ζ 3π/2   0   τ   1

Figure 2-7: A low current beam in strong fields at saturation.

4. High-Current, Strong-Fields and Synchrotron Oscillations

Figure 2-8 corresponds to a high-current beam with j = 10000, the optical wave grows exponentially, as discussed in section D.4, until the onset of saturation. The saturation occurs with similar dynamics as the example of section E.3. However, after saturation and the downward trend of the gain evolution caused by the electron bunch flowing into the $-\pi/2 < \zeta + \phi < \pi/2$ region of phase space, the bunch continues to be driven by the optical wave around the closed orbit inside the separatrix and back into the $\pi/2 < \zeta + \phi < 3\pi/2$ region of phase space. There the electrons transfer their energy back to the optical wave which causes the second increase of the optical power that is seen in the gain evolution. This oscillation in the gain evolution is known as a synchrotron oscillation. Also note how rapidly the optical phase evolves with time.

In Chapter III, it will be shown that the frequency of the synchrotron oscillation is $v_s \approx |a|^{1/2}$. Chapter III will also develop a simple theory using the concept of the a single
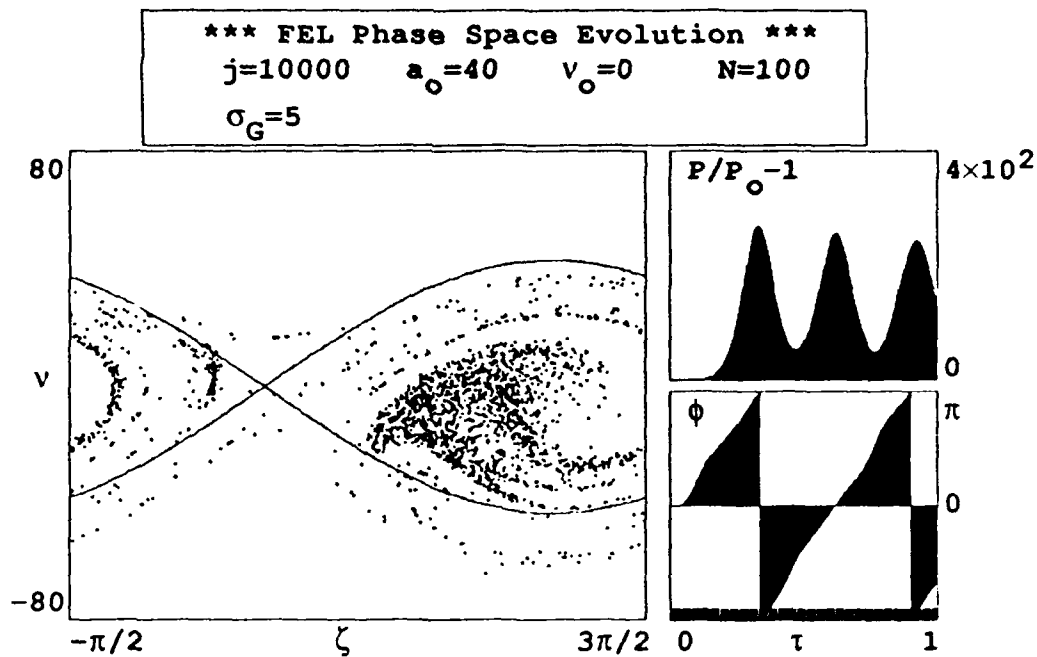
24

Figure 2-8: High currents and strong fields cause synchrotron oscillations due to the electron bunch "sloshing" around phase space following the closed obits in the separatrix.

"macroparticle" to represent the electron bunch. This will allow the development of an approximate solution of the wave and pendulum equations in this highly nonlinear regime.

5. The Tapered Undulator

This example illustrates the effect of tapering an undulator to achieve higher gain. At injection, the electron beam had a Gaussian energy spread with a width of $\sigma_G = 5$, and a current of $j = 2000$. The tapering begins near saturation at $\tau_s \approx 0.6$ with a tapering rate of $\delta = 70\pi$. Note that most of the electrons were trapped inside the separatrix, but that some remain outside the separatrix and are randomized in phase-space. These randomized electrons play a minimal role in the gain mechanism whereas the trapped electrons bunch near the critical point lose energy, and lead to gain. The "sloshing" of the electrons due to synchrotron oscillations is still visible in the gain evolution, but now the closed-orbit area of phase-space is relatively small due to the tapering of the

25

*** FEL Phase Space Evolution ***

j=2000 a_o=10 v_o=0   N=100
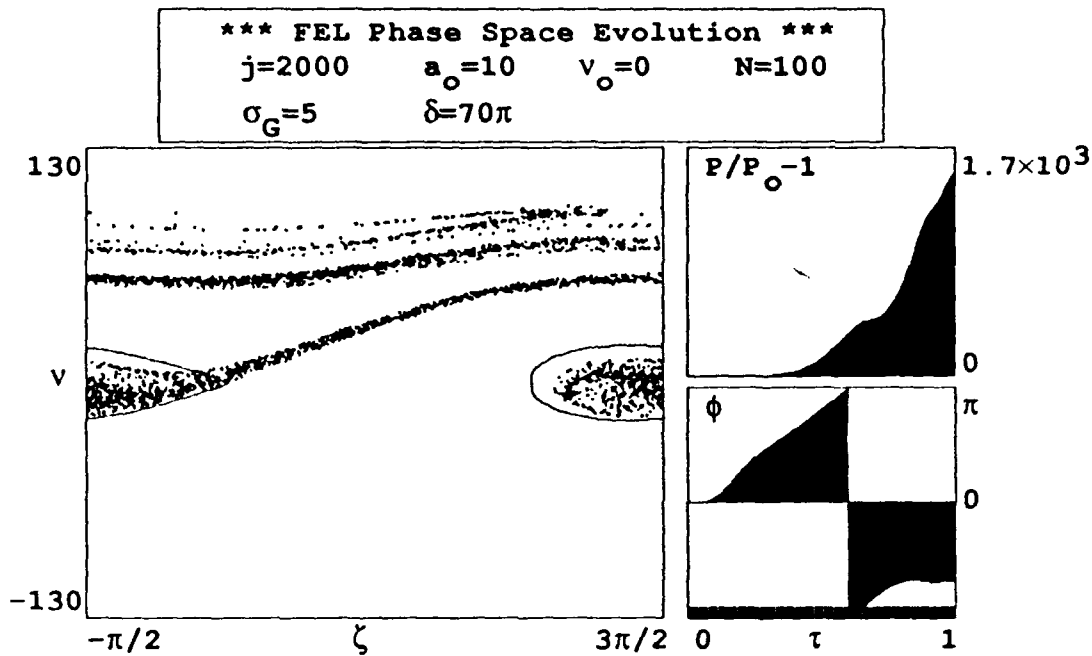
σ_G=5 δ=70π

Figure 2-9: A strongly tapered, high-current undulator.

pendulum equation. This causes the electrons to bunch near $\zeta + \phi \approx 3\pi/2$ so that there is continual growth. The electrons still "slosh", but over a much smaller area of phase-space which is why synchrotron oscillations play a relatively small role in strongly tapered undulators compared to untapered undulators.

26

III MACROPARTICLE MODEL

A. INTRODUCTION

The high-current, strong-field regime of the FEL is highly nonlinear and difficult to analysis quantitatively. However, simple analytic models can be developed by treating the particles trapped in the closed orbit region of phase-space as a single macroparticle. The macroparticle approach was originally developed and used to derive simpler expressions of the pendulum and wave equations that could be used to facilitate FEL design [Ref. 10,11]. The macroparticle approach has also been successfully used to study the stability of Klystron-type FEL's [Ref. 12], and to explore the limits of the pendulum model for FEL dynamics [Ref. 13]. In this chapter, simple solutions to the wave and pendulum equations are derived using the macroparticle approach. The solutions allow quantitative analysis of the optical wave evolution, and provide useful insight into the trapped particle instability.

The macroparticle model presented here is first solved for the tapered undulator where synchrotron oscillations are small. Then a slightly more complex model is developed leading to solutions that describe synchrotron oscillations in the untapered undulator. Comparisons of the simple theory with particle simulations will be interspersed to demonstrate the validity of the model.

B. MACROPARTICLE MODEL

In the high-gain, strong-field regime, the trapped electrons bunch in the closed-orbit region of phase-space allowing them to be treated as a single macroparticle. The untrapped electrons will randomly disperse in phase-space and play a greatly diminished role in the gain mechanism. This removes the required averages from the wave equations and simplifies the system, equations 2-22, 2-35 and 2-36, from 2n + 1 equations to a system of 3 equations,

$$\ddot{\zeta} = \delta\theta(\tau - \tau_s) + |a|\cos(\zeta + \phi) \ , \qquad \text{3-1a}$$

27

$$|\overset{o}{a}| = -j_T \cos(\zeta + \phi) \quad , \qquad \text{3-1b}$$

$$|a|\overset{o}{\phi} = j_T \sin(\zeta + \phi) \quad , \qquad \text{3-1c}$$

where $\theta(\tau - \tau_s)$ is the step function for the tapering constant, δ. The trapped particles are described by a reduced particle current $j_T \approx 0.6j$. The macroparticle remains trapped near resonance, at the bottom of the potential well, so that $\overset{o}{\zeta} \approx 0$.

1. Solutions Without Synchrotron Oscillations

The near-resonance assumption allows for the immediate solution of the pendulum equation, 3-1a, to give $\cos(\zeta + \phi) = -\delta/|a|$. When combined with the wave equations, 3-1b and 3-1c the result is

$$|\overset{o}{a}| = \frac{j_T \delta}{|a|} \quad , \qquad \text{3-2a}$$

$$|a|\overset{o}{\phi} = j_T \left(1 - \frac{\delta^2}{|a|^2}\right)^{1/2} \approx j_T \quad . \qquad \text{3-2b}$$

A properly designed undulator requires $\delta^2 \ll |a|^2$ to insure that there will be closed-orbits that trap the electrons which is consistent with the approximation in 3-2b. The solution to 3-2a is found to be

$$|a(\tau)|^2 = 2j_T\delta(\tau - \tau_s) + |a_s|^2 \quad . \qquad \text{3-3}$$

The solution to 3-2b is found by combining 3-3 with 3-2b and integrating with the appropriate initial conditions yielding

$$\phi(\tau) = |a_s| [(1 + 2j_T\delta(\tau - \tau_s)/|a_s|^2)^{1/2} - 1]/\delta \quad . \qquad \text{3-4}$$

Without tapering the solutions, 3-4 and 3-5, simplify to

$$|a(\tau)|^2 = |a_s|^2 \quad , \qquad \phi(\tau) = \phi_s + \frac{j_T}{|a_s|^2}\tau \quad . \qquad \text{3-5}$$

28

Figure 3-1 illustrates a simulation of a tapered undulator with an initial optical field $a_0 = 10$, a dimensionless current $j = 20000$, and a tapering rate of $\delta = 270\pi$. The electrons are initially placed with a random Gaussian spread in phase velocity related to an energy spread in the electron beam by $4\pi N \Delta\gamma/\gamma \approx \Delta v$. The random Gaussian distribution about v_0 is given by $f_G(q) = \exp[-q^2/2\sigma_G^2]/\sqrt{2\pi}\,\sigma_G$ where the i'th electron's phase velocity is $v_i = v_0 + q$. In Figure 3-1 the width of the distribution is $\sigma_G = 3$. The large left window in the figure is a plot the electron phase-space; electron phase, ζ, versus electron phase velocity, v, where each dot is the electron's final position. Note that the trapped electrons are bunched inside the separatrix while the untrapped electrons were dispersed randomly. The separatrix separates the closed-orbit region of phase-space from the open-orbit region and is plotted as the thin black line in phase-space. The electrons inside the separatrix are bunched near π which causes the continual growth of the power. Synchrotron oscillations are visible as small modulations in the gain evolution and are caused by the "sloshing" of the electrons inside the separatrix. The top-right window plots the power of the FEL
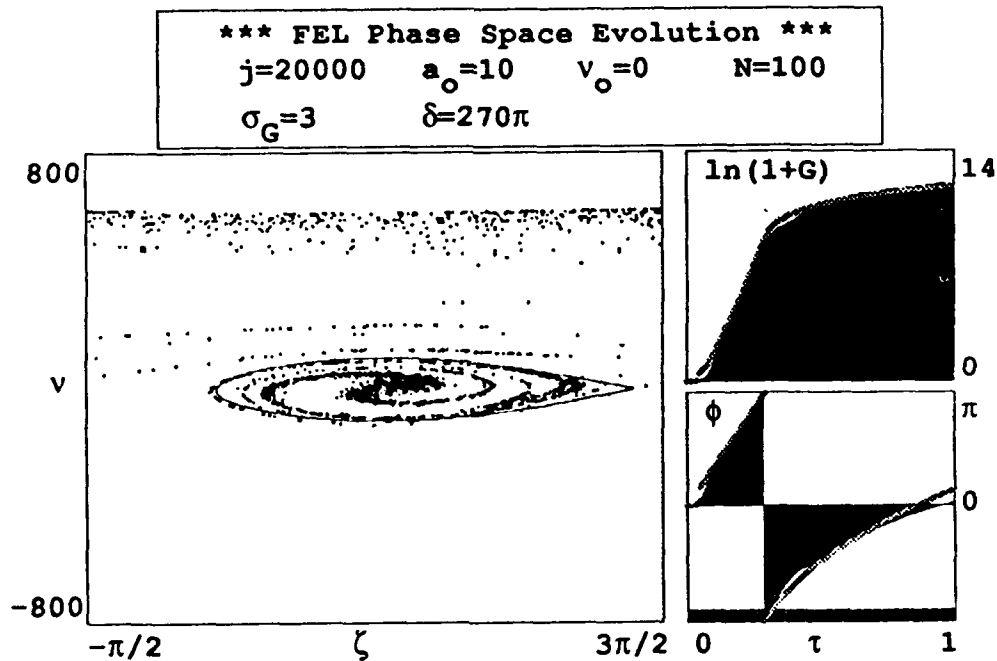

Figure 3-1: High Current, strongly tapered undulator.

over time with the derived analytic solutions superimposed in grey. The simulation's gain evolution is plotted in black. The flat initial portion of the analytical solution, $\tau \approx 0$, and the exponential gain portion, $\tau_{\scriptscriptstyle B} < \tau < \tau_{\scriptscriptstyle J}$, are from the results stated in Chapter II, section D.4. The final portion of the analytical solution is the macroparticle solution that begins after saturation when tapering commences at $\tau \approx 0.3$. Sixty percent of the electrons were assumed trapped in this example. After saturation when tapering commences, the power grows linearly. The bottom-right window plots the evolution of the optical phase with the same three regions of the analytical solution superimposed in grey. Note that the phase grows linearly in time during the exponential growth as predicated. There is close agreement between the analytic solution and the simulation. A gain of $G = 2 \times 10^5$ is achieved.

Figure 3-2 illustrates a tapered undulator with a lower current of $j = 10000$ and a smaller taper rate of $\delta = 200\pi$, but a strong initial optical field $a_0 = 100$. The initial electron beam has a Gaussian spread in phase velocity with a width of $\sigma_G = 5$. Saturation occurs at
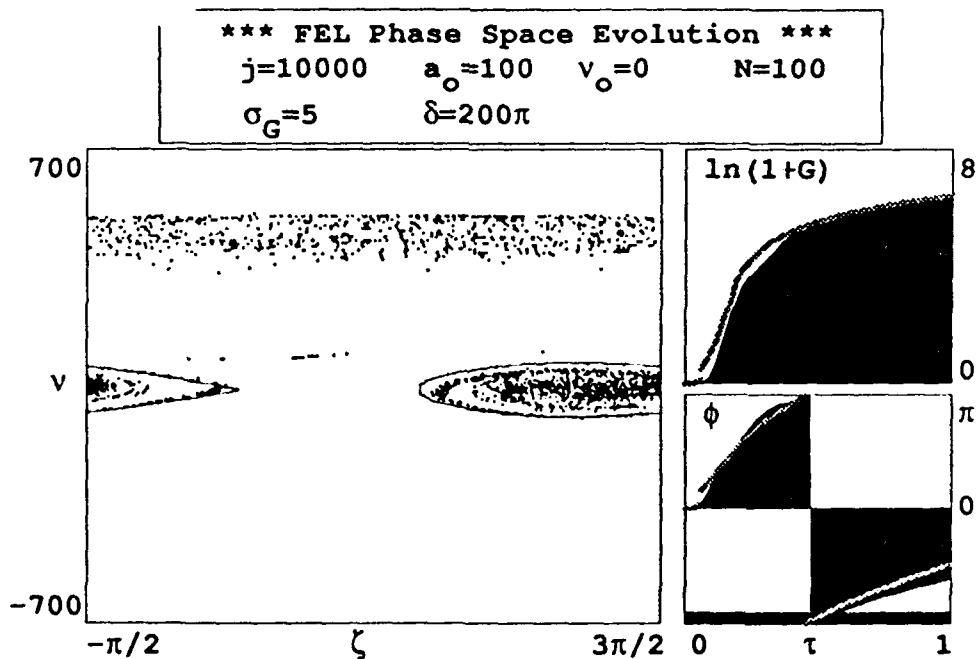

Figure 3-2: High initial field in a strongly tapered undulator.

$\tau_s \approx 0.2$ since the initial field is near saturation. The gain grows linearly after saturation. Figure 3-3 is similar to the simulation of Figure 3-2, but the initial field is much weaker, $a_0 = 10$. This delays saturation until $\tau_s = 0.4$. Both simulations assume $j_r = 0.6j$. In both figures, the simple macroparticle model compares extremely well with the simulations. Synchrotron oscillations are visible in both figures as the small modulation in the gain and phase evolution. The analytic solution

*** FEL Phase Space Evolution ***
j=10000   a$_o$=10   v$_o$=0   N=100
σ_G=5 δ=200π
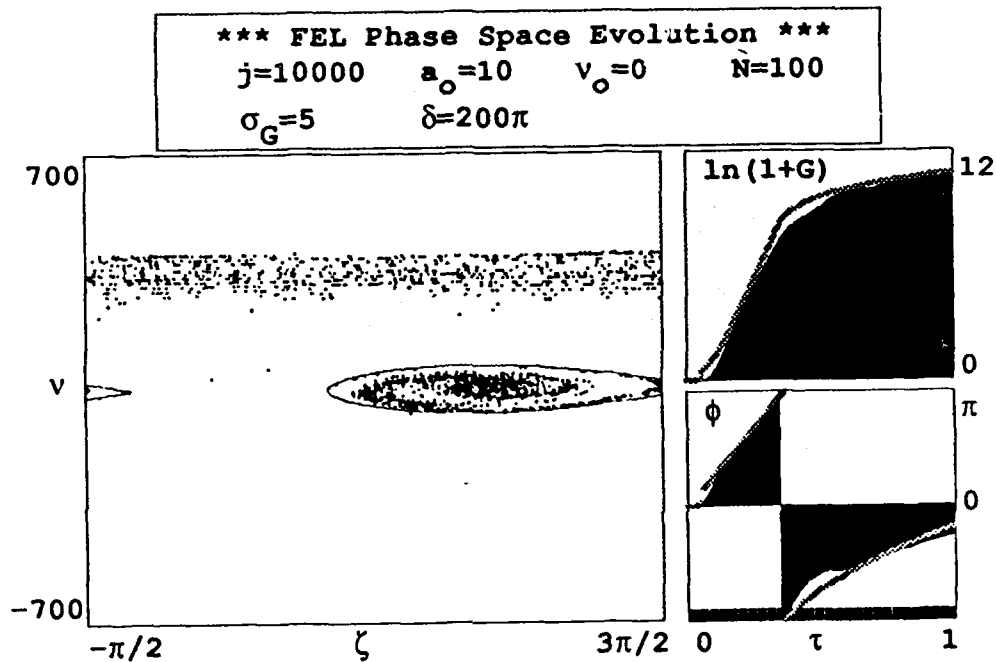
Figure 3-3: Weak initial field in strongly tapered undulator.

can not follow the synchrotron oscillations in the gain evolution since the analytic solution assumed that the macroparticle was rigidly trapped at the bottom of the optical potential well. However, the macroparticle can oscillate slightly as is evident by the closed orbits inside the separatrix and the slight modulation of the gain evolution. With tapered undulators, these oscillations are relatively small and can be ignored. In untapered undulators, synchrotron oscillations are substantially more pronounced and must be accounted for. The next section will account for the oscillations of the macroparticle in the potential well and accurately predict the synchrotron oscillations.

31

Figure 3-4 shows a simulation with parameters similar to the LLNL ELF experiment, but with better beam quality [Ref. 14]. The dimensionless current is $j = 7000$ with a random phase-velocity spread of width $\sigma_+ = 3$. The initial optical field is $a_0 = 12$, and the taper rate is $\delta = 80\pi$. Again, the analytic solution closely follows the simulation. The simulation and the analytic solution both show efficiency of about 30% which compares well with the experiment.
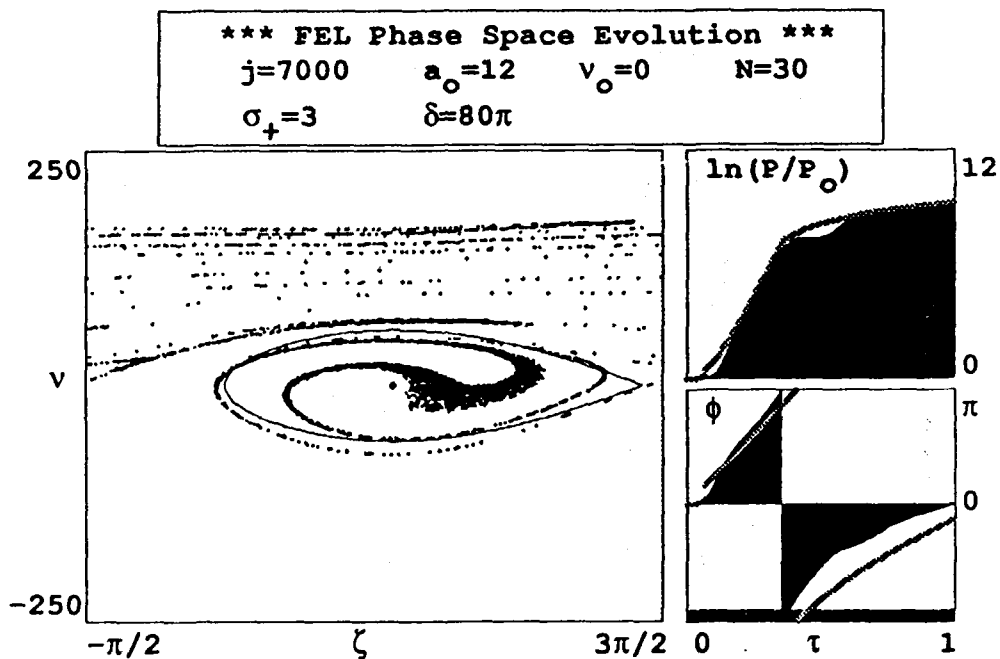

Figure 3-4: A simulation of an FEL with parameters close to LLNL ELF is compared with the macroparticle model.

2. Solutions with Synchrotron Oscillations

The macroparticle model can be extended to include synchrotron oscillations for untapered undulators, $\delta = 0$, where the effect of synchrotron oscillations is more pronounced. With the assumption that the macroparticle is trapped at the bottom of the optical potential well, $\ddot{\zeta} \approx 0$, the pendulum equation, 3-1a, can be solved for an equilibrium position

$$\zeta^* = \frac{\pi}{2} - \phi \quad . \tag{3-6}$$

The macroparticle is now allowed to oscillate near the bottom of the optical potential well, around ζ^* so that

$$\zeta \approx \zeta^* + x(\tau) = \frac{\pi}{2} - \phi + x(\tau) \quad , \tag{3-7}$$

where $x(\tau) \ll \pi$. Assuming that the optical field does not change rapidly after saturation, $|\overset{\circ}{a}| \approx \overset{\circ}{\phi} \approx 0$, the solution for $x(\tau)$ can be found by combining 3-7 with the pendulum equation 3-1a. Using a small angle approximation for $x(\tau)$ yields

$$\overset{\circ\circ}{\zeta} = \overset{\circ\circ}{x} = |a_s| \cos(\zeta^* + x(\tau) + \phi) \approx -|a_s| x(\tau) \quad , \tag{3-8}$$

where $|a_s|$ was substituted for $|a|$ since $|a|$ is nearly constant after saturation. Equation 3-8 has a solution of

$$x(\tau) = \zeta_0 \cos(\nu_s(\tau - \tau_s)) \quad . \tag{3-9}$$

The frequency of the synchrotron oscillation is $\nu_s = |a_s|^{1/2}$. The initial conditions for the macroparticle in phase-space are determined phenomenologically by comparing with simulations. The best solution is found to be $\zeta_0 \approx 0.6$ and $\nu_0 = 0$ as expressed in 3-9.

Combining 3-7 with 3-1b yields

$$\begin{aligned} |\overset{\circ}{a}| &= -j_T \cos(\zeta^* + x(\tau) + \phi) \\ &\approx j_T x(\tau) \quad , \end{aligned} \tag{3-10}$$

after the small angle approximation is applied. Combining 3-9 and 3-10 produces a solution for the optical field strength

$$|a(\tau)| = \frac{j_T \zeta_0}{\nu_s} \sin(\nu_s (\tau - \tau_s)) + |a_s| \quad . \tag{3-11}$$

33

Combining the optical phase expression of 3-2b with the new optical field strength solution from 3-11 gives

$$\phi(\tau) = \phi_s + \frac{j_T}{|a_s|}(\tau - \tau_s) + \frac{j^2 \zeta_0}{|a_s|^2 v_s^2}\cos(v_s(\tau - \tau_s)) \quad , \qquad 3\text{-}12$$

after expanding to first-order in $x(\tau)$ and integrating.

Figures 3-5 and 3-6 compare the improved macroparticle model for untapered undulators with simulations using current $j = 1000$, and initial optical fields of $|a_0| = 1$ and $|a_0| = 30$ respectively. These examples illustrate the macroparticle model's excellent ability to predict the onset of saturation. Both simulations use nearly monoenergetic beams described by $\sigma_G = 1$ with 1000 sample electrons and 300 time steps. Note that in Figure 3-5, the FEL just saturates, whereas in Figure 3-6, the FEL saturates and undergoes nearly two synchrotron oscillations. This is due to the high initial field that causes saturation to happen at a much earlier time.
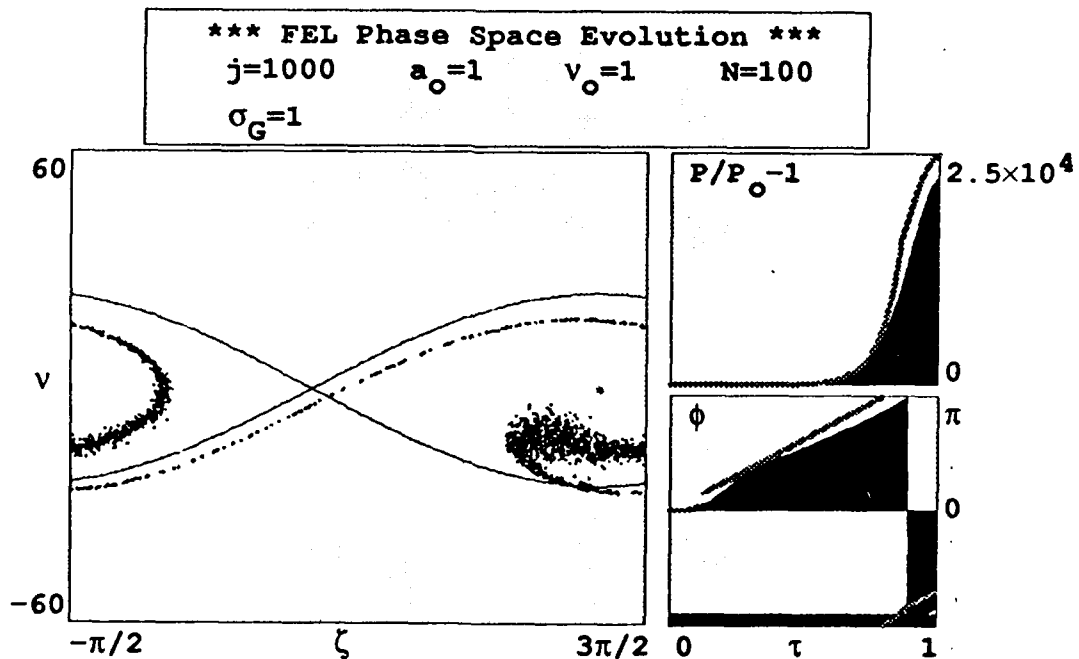
Figure 3-5: A comparison of the macroparticle model's solutions with a weak initial field simulation and current j = 1000.

*** FEL Phase Space Evolution ***
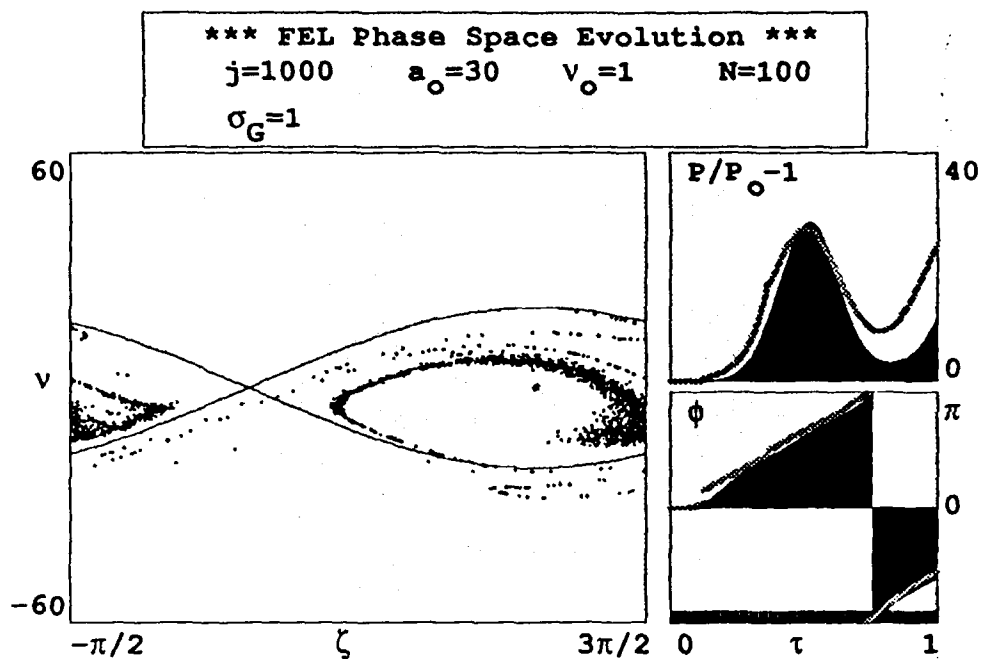$j=1000$ $a_o=30$ $v_o=1$ $N=100$
$\sigma_G=1$

Figure 3-6: A comparison with higher initial fields and a current of j = 1000.

Figures 3-7 and 3-8 demonstrate the macroparticle model capabilities with much higher currents of $j = 10000$, and initial fields of $|a_0| = 10$ and $|a_0| = 100$. Both simulations have nearly monoenergetic beams, $\sigma_G = 1$, with 1000 sample particles, use 600 time steps, and assume sixty percent of the electrons are trapped. In both examples, the macroparticle model predicts saturation very well and follows the synchrotron oscillation. The analytic optical phase solutions also follow the simulation closely and show the synchrotron oscillations. With the higher initial field, saturation occurs sooner.

Figure 3-9 shows a simulation of an untapered undulator with a much higher current of $j = 20000$, and nearly perfect beam quality, $\sigma_G = 1$. Note the very tight bunch inside the separatrix even after nearly four synchrotron oscillations. Once again the analytic solution follows the simulation closely, but the predicted synchrotron frequency is slightly higher than in the actual simulation. Note that the analytic power solution, $P(\tau)$, after saturation is sinusoidal but in the
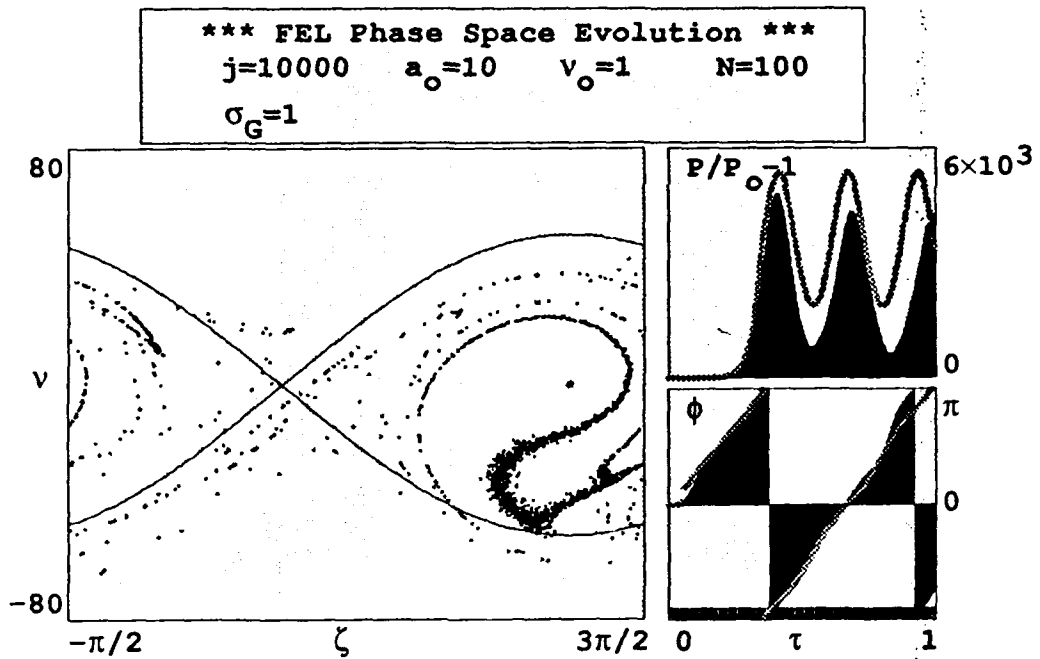
35

Figure 3-7: High current with 3 synchrotron oscillations.

simulation the synchrotron oscillations are not exactly sinusoidal. This is due to the assumption that $|\overset{\circ}{a}| \approx 0$ after saturation which is not completely accurate. In the simulations, the peaks of the power curve are sharper than the troughs since $|a(\tau)|$ is not completely constant as was assumed. In Figure 3-10, Coulomb affects have been examined for this example and appear to have little effect on the theory.

As a final example, Figure 3-11 shows the comparison between the solutions of 3-7 and 3-8 and a simulation using 5000 electrons that has parameters similar to the LLNL ELF untapered undulator [Ref. 15]. The initial field strength is $|a_0| = 10$, the dimensionless current is $j = 3350$ and the random phase-velocity spread is $\sigma_+ = 3$. From the power evolution, $P(\tau)$,
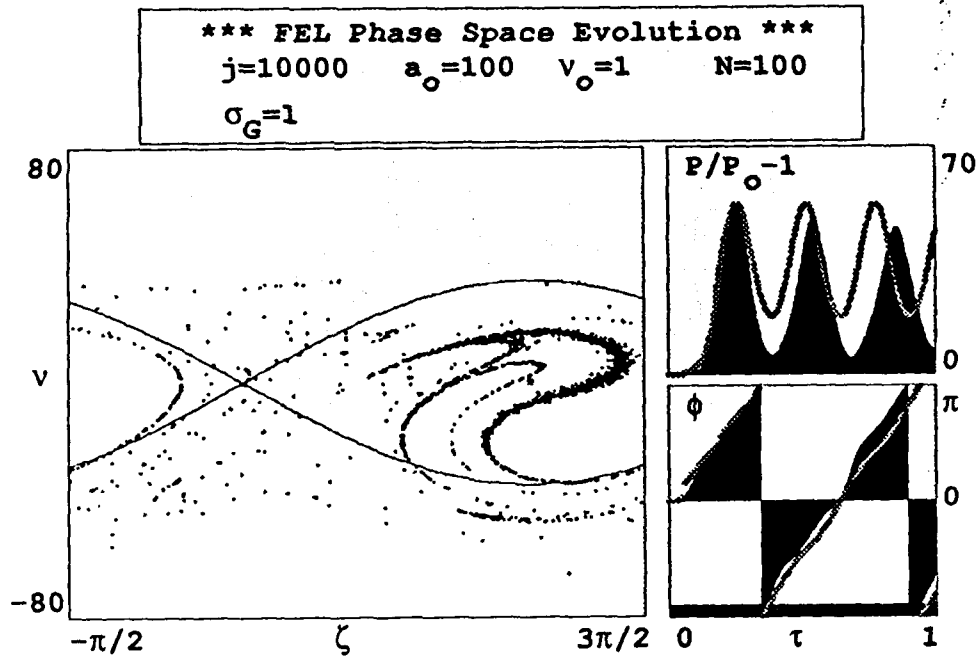
Figure 3-8: Higher initial field causes saturation to occur sooner.

it is apparent that the electrons undergo about two synchrotron oscillations, and that the analytic solution closely follows the simulation. The analytic phase solution also shows synchrotron *oscillations as it follows the simulation.*

C.   CONCLUSION

The macroparticle model provides simple analytic solutions to FEL dynamics in the highly non-linear regime with high-currents and strong-fields. The results could provide the necessary tools to lead to multimode theoretical studies of the trapped-particle instability, sideband development and chaos in the FEL. Such simple analytic results can be used in the design of future high-power, high-gain FEL's.
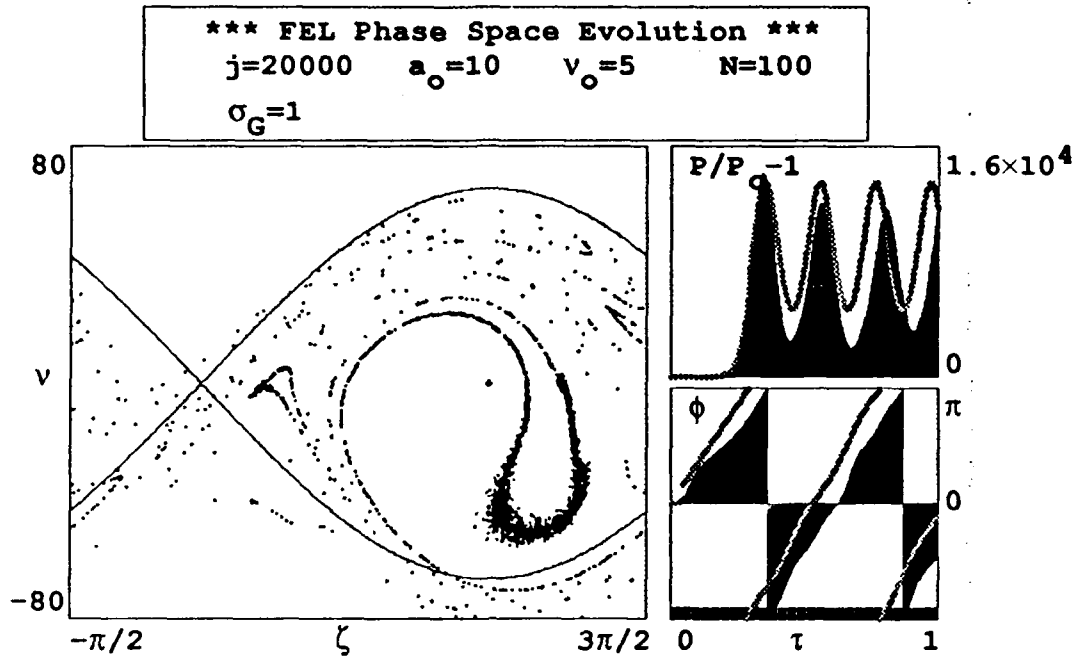
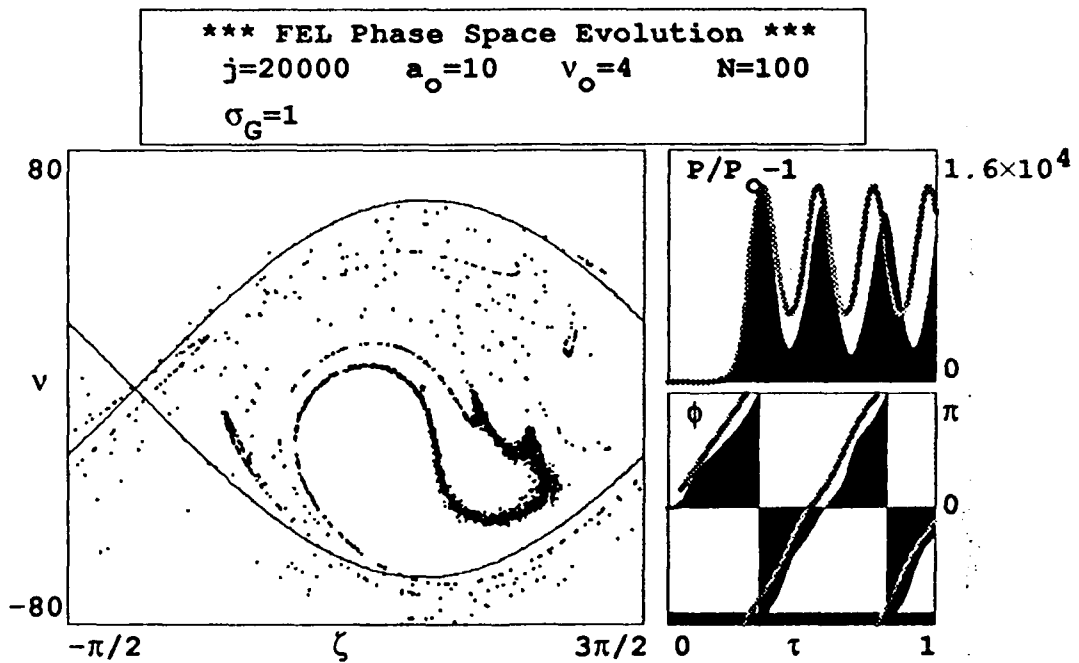Figure 3-9: A high current example, j = 20000, with four synchrotron oscillations.

Figure 3-10: A high current FEL with many synchrotron oscillations compared to the macroparticle model with Coulomb affects considered.
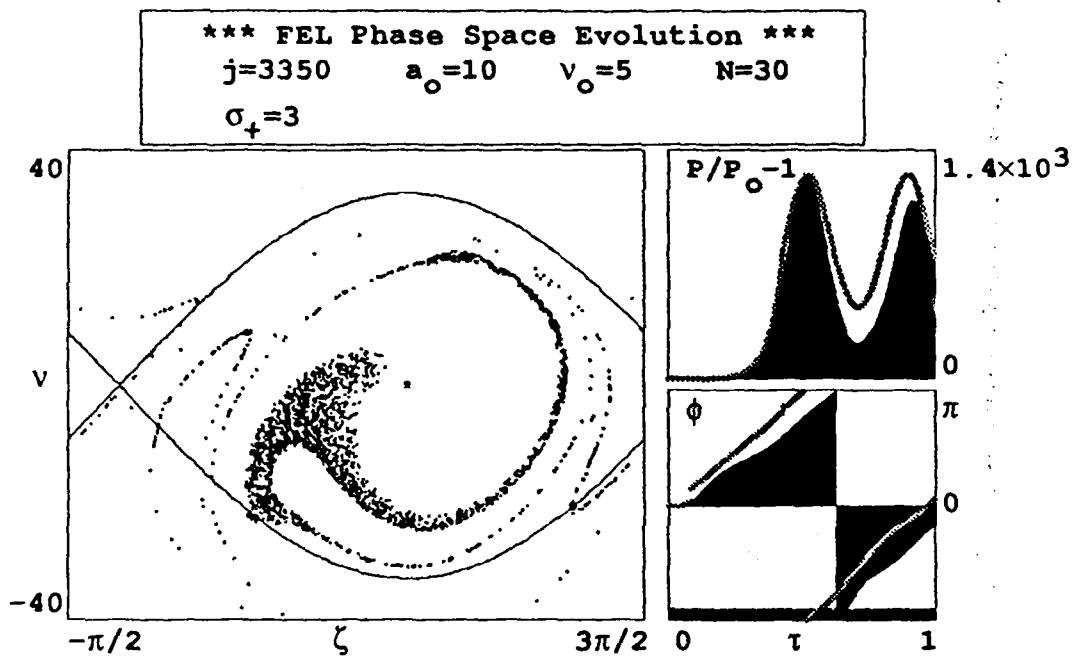
Figure 3-11: Macroparticle model compared with untapered undulator that has parameters close to the LLNL ELF FEL.

IV TWO MODE THEORY

A. INTRODUCTION

In the FEL oscillator, the optical evolution can develop sidebands and become highly chaotic over many low gain passes just as the FEL amplifier can develop sidebands and chaotic behavior over one high gain pass. This highly non-linear behavior in the FEL oscillator is difficult to analyze due to the complexity that arises from the multiple longitudinal optical modes interacting with the electrons. One of the consequences of this nonlinear behavior is the trapped particle instability which can be analyzed through longitudinal, multi-mode analysis [Ref. 16-21]. In this chapter, a simpler model will be developed that limits the number of modes in the oscillator to two, which is sufficiently simple to study the stability of the FEL oscillator, but not excessively simple so as to be unrealistic. The two-mode model presented here will provide a valuable tool to study long term stability of the optical wave, the development of sidebands and the onset of chaos in a FEL oscillator.

B. ELECTRON AND OPTICAL DYNAMICS

To study the electron and optical dynamics in the oscillator with two optical modes present, equations of motion for the electrons must be developed and then used to derive the driving current in the optical wave equation. This can be accomplished in a manner analogous to the derivation of the pendulum and wave equations of Chapter II, producing two-mode pendulum and wave equations. These two-mode wave and pendulum equations will then be used in computer simulations to explore stability in the FEL oscillator.

1. Electron Dynamics and the Two-mode Pendulum Equation

The derivation of the two-mode pendulum equation is very similar to the single mode pendulum equation of Chapter II, so only a sketch of the two-mode pendulum equation derivation will be presented. With two optical modes present, the electron equations of motion are

$$\frac{d(\gamma \vec{\beta})}{dt} = -\frac{e}{mc}(\vec{E} + \vec{E}_s + \vec{\beta} \times (\vec{B}_m + \vec{B} + \vec{B}_s)) \quad , \qquad \text{4-1a}$$

$$\frac{d\gamma}{dt} = -\frac{e}{mc} \vec{\beta} \cdot (\vec{E} + \vec{E}_s) \quad , \qquad \text{4-1b}$$

where $\vec{E}$ and $\vec{B}$ are the electric and magnetic fields of the primary optical field, and $\vec{E}_s$ and $\vec{B}_s$ are the electric and magnetic fields of the secondary optical field. The charge and mass of the electron are denoted by e and m, and c is the speed of light. The undulator's magnetic field is denoted by $\vec{B}_m$. Assume that the primary optical field is of the form

$$\vec{E} = E(\cos\psi, -\sin\psi, 0) \quad , \quad \vec{B} = E(\sin\psi, \cos\psi, 0) \quad , \qquad \text{4-2}$$

and the secondary field is of the form

$$\vec{E}_s = E_s(\cos\psi_s, -\sin\psi_s, 0) \quad , \quad \vec{B}_s = B(\sin\psi_s, \cos\psi_s, 0) \quad , \qquad \text{4-3}$$

where $\psi = kz - \omega t + \phi$ and $\psi_s = k_s - \omega_s t + \phi_s$, k and k_s are the wave numbers, ω and ω_s are the frequencies, and ϕ and ϕ_s are the phases of their respective optical waves. Also assume the undulator field is helical of the form

$$\vec{B}_m = B_m(\cos(k_0 z), \sin(k_0 z), 0) \quad , \qquad \text{4-4}$$

where k_0 is the wave number of the undulator's magnetic field and z is the longitudinal coordinate for the long axis of the undulator.

Substitute 4-2, 4-3 and 4-4 into the equations of motion, 4-1, and solve for the perpendicular motion as in the derivation of the pendulum equation in Chapter II. Use of the approximations, $|\vec{E}|(1 - \beta_z) \ll |\vec{B}_m|$ and $|\vec{E}_s|(1 - \beta_z) \ll |\vec{B}_m|$ [Ref. 8] gives

$$\vec{\beta}_\perp = -\frac{K}{\gamma}(\cos(k_0 z), \sin(k_0 z), 0) \quad , \qquad \text{4-5}$$

where $K = eB_m/2\pi mc^2$ is the undulator parameter. The energy equation is

41

$$\frac{d\gamma}{dt} = \frac{e}{mc}\frac{K}{\gamma}(E\cos(k_o z + \psi) + E_s\cos(k_o z + \psi_s)) \quad . \qquad \text{4-6}$$

Now a relation between the electron's phase with respect to the optical wave and $\dot\gamma$ needs to be derived. As in the single mode pendulum equation, start with $\gamma^{-2} = 1 - \beta_\perp^2 - \beta_z^2$. Using the perpendicular motion solved for in 4-5, solve for β_z yielding

$$\beta_z \approx 1 - \frac{(1 + K^2)}{2\gamma^2} \quad , \qquad \text{4-7}$$

since the electrons are relativistic. Taking the time derivative yields

$$\dot\beta_z = \frac{(K^2 + 1)}{\gamma^2}\frac{\dot\gamma}{\gamma} \quad . \qquad \text{4-8}$$

Now define the electron phase with respect to the primary optical wave so that $\zeta = (k + k_0)z - \omega t$. Taking the second time derivative of ζ yields

$$\dot\beta_z = \frac{\ddot\zeta}{(k + k_0)c} \quad , \qquad \text{4-9}$$

when solved for $\dot\beta_z$.

Equating 4-8 and 4-9, and using the resonance condition $\lambda_0/2\lambda = \gamma^2/(1 + K^2)$ gives

$$\dot\gamma = \frac{\gamma\ddot\zeta}{(k + k_0)c}\frac{k}{2k_0} \approx \frac{\gamma\ddot\zeta}{2k_0 c} \quad , \qquad \text{4-10}$$

since $k_0 < k$. Equating 4-6 and 4-10, combining with the definition of ζ and introducing the dimensionless time $\tau = ct/L$ and dimensionless optical fields $|a| = 4\pi NKeLE/\gamma^2 mc^2$ and $|a_s| = 4\pi NeKLE_s/\gamma^2 mc^2$ gives the two-mode pendulum equation

$$\overset{\circ}{v} = \overset{\circ\circ}{\zeta} = |a|\cos(\zeta + \phi) + |a_s|\cos(k_o z + \psi_s) \quad . \qquad \text{4-11}$$

As before, "$\circ$" denotes $d/d\tau$. The z dependence in the pendulum equation can be eliminated by using the approximation $k, k_s > k_0$ and the definition $\Delta v_s = ((k - k_s)/k)2\pi N = ((\lambda_s - \lambda)/\lambda_s)2\pi N$ where N is the number of undulator periods. This gives

$$\overset{\circ\circ}{\zeta} = |a|\cos(\zeta + \phi) + |a_S|\cos(\zeta + \Delta v_S \tau + \phi_S) \quad . \qquad \text{4-12}$$

Normally Δv_s is between 2π and 10π since the areas of interest are $(\lambda_s - \lambda)2\pi N/\lambda \approx a^{1/2}$ which is the typical range of synchrotron oscillations. It is interesting to note that by defining ζ with respect to the carrier wave (k,ω), the symmetry of the two-mode equation is broken.

2. Optical Wave Evolution and the Two-Mode Wave Equation

The two-mode wave equation is derived in the same manner as the single mode wave equation. The optical fields of 4-2 and 4-3 have the vector potential

$$\vec{A} = \frac{E}{k}(\sin\psi,\cos\psi,0) + \frac{E_s}{k_s}(\sin\psi_s,\cos\psi_s,0) \quad . \qquad \text{4-13}$$

Substituting 4-13 into the general wave equation 2-24 and applying the slowly varying amplitude and phase approximations (SVAP) to eliminate all terms with two derivatives yields the left hand side of the wave equation

$$\left(\vec{\nabla}^2 - \frac{1}{c^2}\frac{\partial^2}{\partial t^2}\right)\vec{A} = \frac{2}{c}\dot{E}(\cos\psi,-\sin\psi,0)$$

$$- \frac{2}{c}E\dot{\phi}(\sin\psi,\cos\psi,0) \qquad \text{4-14}$$

$$+ \frac{2}{c}\dot{E}_S(\cos\psi_s,-\sin\psi_s,0)$$

$$- \frac{2}{c}E_S\dot{\phi}_S(\sin\psi_s,\cos\psi_s,0) \quad .$$

The rapidly rotating ψ terms of 4-14 can be eliminated by defining four polarization vectors

$$\hat{\varepsilon}_1 = (\cos\psi,-\sin\psi,0) \qquad \hat{\varepsilon}_2 = (\sin\psi,\cos\psi,0)$$
$$\hat{\varepsilon}_{S1} = (\cos\psi_s,-\sin\psi_s,0) \qquad \hat{\varepsilon}_{S2} = (\sin\psi_s,\cos\psi_s,0) \qquad \text{4-15}$$

to project into the wave equation producing four equations

43

$$\frac{2}{c}(\dot{E} + \dot{E}_S\cos(\psi - \psi_S) + E_S\dot{\phi}_S\sin(\psi - \psi_S)) = \frac{4\pi}{c}\vec{J}_\perp \cdot \hat{e}_1$$

$$\frac{2}{c}(-E\dot{\phi} + \dot{E}_S\sin(\psi - \psi_S) - E_S\dot{\phi}_S\cos(\psi - \psi_S)) = -\frac{4\pi}{c}\vec{J}_\perp \cdot \hat{e}_2$$

$$\frac{2}{c}(\dot{E}\cos(\psi - \psi_S) - E\dot{\phi}\sin(\psi - \psi_S) + \dot{E}_S) = -\frac{4\pi}{c}\vec{J}_\perp \cdot \hat{e}_{S1}$$

$$-\frac{2}{c}(\dot{E}\sin(\psi - \psi_S) - E\dot{\phi}\cos(\psi - \psi_S) - E_S\dot{\phi}_S) = -\frac{4\pi}{c}\vec{J}_\perp \cdot \hat{e}_{S2}$$

4-16

Now the right side of the general wave equation needs to be developed to find the transverse beam current. Since a single particle has a transverse current, $\vec{J}_{\perp J} = -ec\vec{\beta}_\perp \delta^{(3)}(\vec{x} - \vec{r}_j)$ [Ref. 9], giving $\vec{J}_{\perp J} = (ecK/\gamma)(\cos k_0 z, \sin k_0 z, 0)\delta^{(3)}(\vec{x} - \vec{r}_j)$ when combined with the transverse electron motion, 4-5. Projecting each of the four polarization vectors into the single particle current yields

$$\vec{J}_{\perp J} \cdot \hat{e}_1 = \frac{ecK}{\gamma}\cos(k_0 z + \psi)\delta^{(3)}(\vec{x} - \vec{r}_j)$$

$$\vec{J}_{\perp J} \cdot \hat{e}_2 = \frac{ecK}{\gamma}\sin(k_o z + \psi)\delta^{(3)}(\vec{x} - \vec{r}_j)$$

4-17

$$\vec{J}_{\perp J} \cdot \hat{e}_{S1} = \frac{ecK}{\gamma}\cos(k_0 z + \psi_s)\delta^{(3)}(\vec{x} - \vec{r}_j)$$

$$\vec{J}_{\perp J} \cdot \hat{e}_{S2} = \frac{ecK}{\gamma}\sin(k_0 z + \psi_s)\delta^{(3)}(\vec{x} - \vec{r}_j)$$

Summing the single particle currents, 4-17, over all the particles, equating with the left hand side of the wave equation, 4-16 and multiplying each of the four resultant equations of motion with $4\pi NeKL^2/\gamma^2 mc^3$ yields

$$|\overset{o}{a}| + |\overset{o}{a}_s|\cos(\Delta v_s\tau + \phi_s - \phi) - |a_s|\overset{o}{\phi}_s\sin(\Delta v_s\tau + \phi_s - \phi) = -j\langle\cos(\zeta + \phi)\rangle$$

$$|a|\overset{o}{\phi} + |\overset{o}{a}_s|\sin(\Delta v_s\tau + \phi_s - \phi) + |a_s|\overset{o}{\phi}_s\cos(\Delta v_s\tau + \phi_x - \phi) = j\langle\sin(\zeta + \phi)\rangle$$

$$|\overset{o}{a}|\cos(\Delta v_s\tau + \phi_s - \phi) + |a|\overset{o}{\phi}\sin(\Delta v_s\tau + \phi_s - \phi) + |\overset{o}{a}_s| = -j\langle\cos(k_0 z + \phi_s)\rangle$$

$$-|\overset{o}{a}|\sin(\Delta v_s\tau + \phi_s - \phi) + |a|\overset{o}{\phi}\cos(\Delta v_x\tau + \phi_s - \phi) + |a_s|\overset{o}{\phi}_s = j\langle\sin(k_0 z + \psi_s)\rangle$$

4-18

when the dimensionless time τ is introduced and j is the dimensionless current defined as before. Multiplying the second and fourth equations of 4-18 by i and then combining the first and the

44

second, and the third and the fourth equations yields the two-mode wave equations

$$\overset{\circ}{a} + \overset{\circ}{a}_s e^{i\Delta v_s \tau} = -j\langle e^{-i\zeta}\rangle$$

$$\overset{\circ}{a} + \overset{\circ}{a}_s e^{i\Delta v_s \tau} = -j\langle e^{-i(1 - \Delta v_s/2\pi N)\zeta)}\rangle$$

4-19

since $k_0 + \psi_s = (1 - \Delta v_s/2\pi N)\zeta(\tau) + \Delta v_s\tau + \phi_s$. Consistency between the two equations of 4-19 requires $\Delta v_s \ll 2\pi N$. This eliminates the second of the equations in 4-19 so that there is only one wave equation to follow

$$\overset{\circ}{a} + \overset{\circ}{a}_s e^{i\Delta v_s \tau} = -j\langle e^{-i\zeta}\rangle$$

4-20

3. Computer Implementation of Two-mode Theory

The two-mode wave equation, 4-20, is not immediately implementable for computer simulation since the two-modes need to be separated into two separate equations. To separate a from a_s in 4-20, one simplifying approximation must be made, the gain over a single pass will be small. This limits the two-mode theory to FEL oscillators with low single pass gain since amplifiers have large gain over one pass. This approximation allows the wave equation to be integrated over time to eliminate one of the optical terms. Before separating the two optical terms in 4-20, a value for Δv_s must be established. Since the sideband is the mode that is modulating the carrier wave, and is produced by the synchrotron oscillations, it will have a frequency that is different from the carrier wave by 2π, the frequency of one synchrotron oscillation. Therefore $\Delta v_s \approx 2\pi$.

To separate the two-modes out of 4-20, integrate 4-20 over time τ from 0 to 1 using the two approximations above. This yields

4-21

$$\Delta a = -j\langle \int_0^1 e^{-i\zeta(\tau)}d\tau\rangle \quad .$$

To find the change in the sideband, multiply 4-20 by $e^{-i2\pi\tau}$ and integrate over time again yielding

$$\Delta a_s = -j\langle \int_0^1 e^{-i(\zeta + 2\pi\tau)}d\tau\rangle \quad .$$

4-22

45

Since it is easier to deal with real rather than complex numbers in computers, equations 4-21 and 4-22 can be broken into real and imaginary parts by application of Euler's theorem yielding

$$\Delta a_r = -j \int_0^1 \langle \cos\zeta \rangle d\tau$$

$$\Delta a_I = j \int_0^1 \langle \sin\zeta \rangle d\tau$$

$$\Delta a_{SR} = -j \int_0^1 \langle \cos(\zeta + 2\pi\tau) \rangle d\tau \qquad\qquad \text{4-23}$$

$$\Delta a_{SI} = j \int_0^1 \langle \sin(\zeta + 2\pi\tau) \rangle d\tau \quad .$$

Similarly, the two-mode pendulum equation, 4-12, can be broken into its real and imaginary parts

$$\ddot{\zeta} = \delta + a_R \cos\zeta - a_I \sin\zeta + a_{SR} \cos(\zeta + 2\pi\tau) - a_{SI} \sin(\zeta + 2\pi\tau) \quad , \qquad \text{4-24}$$

where δ is the tapering constant or artificial acceleration applied to the electrons after saturation in order to maintain resonance. Unlike an FEL amplifier, the tapering constant is always on in a FEL oscillator if there is to be tapering applied.

The program to implement the two-mode model is now straight forward. There are three main loops. The first, inner most, loop integrates the pendulum equation, 4-24, over all the electrons and keeps a sum of $\cos\zeta_i$ and $\cos(\zeta_i + 2\pi\tau)$ to be used as the averages in the wave equation. The next outer loop is the time loop repeated for each time step of a single pass. It integrates the wave equations using the averages produced by the inner most electron loop. The averages are reset for each time step. The outermost loop is the pass loop that controls the number of passes through the undulator. At the end of each pass, the optical wave is attenuated by the oscillator Q factor.

4. Simple Oscillator Model

For low-currents and weak-fields, the gain can be calculated from 2-42 as approximately $G = 0.135\, j$ for $v_0 = 2.6$ for each pass through the undulator. For many passes, the power will be $P = P_0 e^{jn}$

where n is the number of passes. The loss of optical power due to cavity losses is related to the "Q" factor of the oscillator so that over many passes the power in the oscillator will be

$$P = P_0 \exp(0.135jn - n/Q) = P_0 \exp(0.135jQ - 1)n/Q \quad . \qquad 4\text{-}25$$

From this simple model, any combination of $jQ = C1$ and $n/Q = C2$, where $C1$ and $C2$ are constants, will scale the power and phase evolutions to look identical after n passes. With this simple model, many different combinations of n, j and Q can be explored with one simulation.

C. RESULTS OF COMPUTER SIMULATION OF TWO-MODE MODEL

1. Comparison with Existing Simulations

In order to establish the validity of the two-mode model and the correctness of its integration routine, simulations using the two-mode model over one pass are compared with existing simulations known to give correct results over one pass. Figure 4-1 and 4-2 compare the two-mode model with the single-mode model used to produce the earlier FEL simulations. In both figures, the large window is the phase-space evolution of the electrons with the final phase-space position plotted at the end of the undulator pass. Over one pass, the evolution of the second mode will not have a significant affect on the power, phase or electron phase-space evolution if it is started at zero power since it does not grow significantly. From Figure 4-1 and 4-2, it is apparent that the phase-space evolution is nearly identical. The optical power and phase in both simulations produce nearly the same final powers and phase. From this comparison it can be seen that the two-mode's integration technique is probably correct.

The two-mode model can be compared with a much more sophisticated model to demonstrate that the two-mode model accurately predicts the onset of a single sideband. Figure 4-3 shows a simulation of the two-mode model for $j = 5$ and $Q = 7$ over 1000 passes. Note how quickly the main mode grows, saturates, and has a decaying oscillation. The sideband has a similar

47

```
*** FEL Phase Space Evolution ***
j=1          a_o=1      v_o=2.6   N=100
σ=0
```
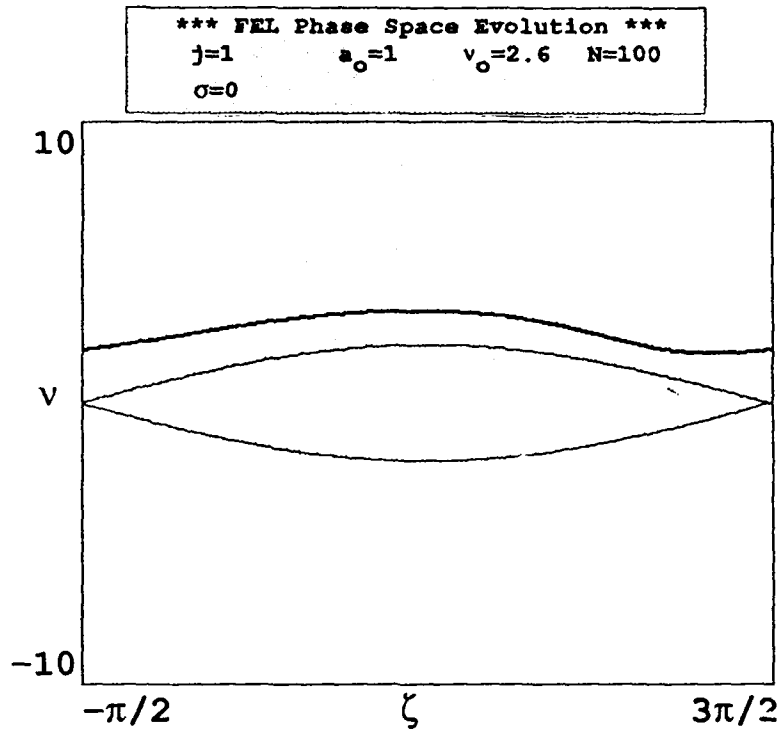
Figure 4-1: Single-mode simulation for comparison with the two-mode model.

pattern but oscillates about a much lower power, about 1/5 the power of the main mode. Figure 4-4 is a multi-mode simulation where each mode is freely allowed to evolve at its natural frequency. This simulation has a random fluctuation with a rms value of $\delta a = 5$ added to the initial optical field strength to simulate noise in the optical wave. The left-center window displays the evolution of the optical power, $|a(z,n)|$, over 1000 passes through a gray scale where black is $|a(z)| = 0$ and white represents $|a(z)| = 25.5$ with a contour line at $|a(z)| = 12.8$. The window has a width of two slippage distances with periodic boundary conditions. The slippage distance is the interaction distance that the electrons can couple with the optical wave. The slippage distance is the distance that the optical wave gains over the electron pulse while overtaking it during the trip down the undulator and is given by, $N\lambda$, where N is the number of undulator periods and λ is the wavelength of the main lobe of the optical wave. For each pass, the electrons start almost uniformly spread in phase-space

48
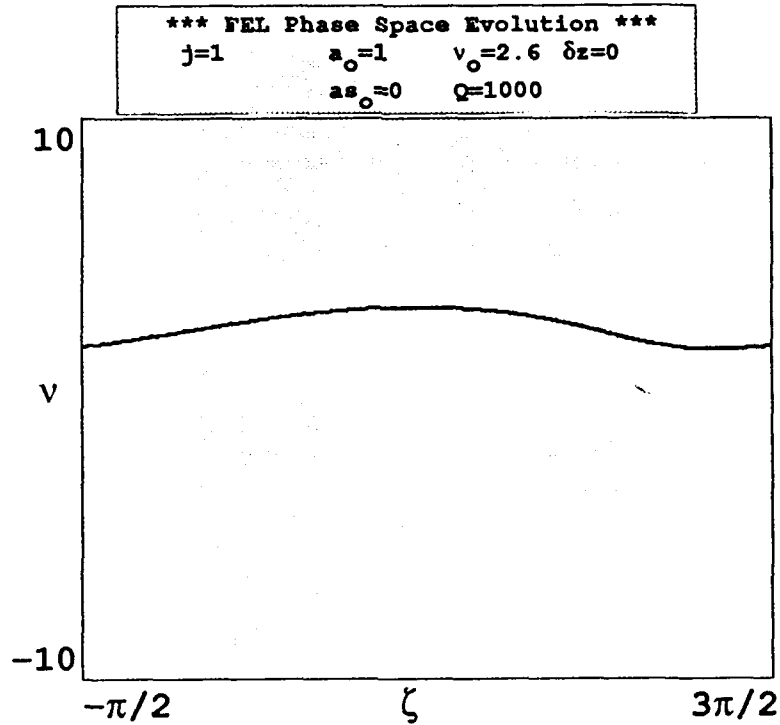
Figure 4-2: Two-mode model for comparison with figure 4-1.

at each site along z, but have a small random displacement in phase where a rms spread of $\delta\zeta = 0.0001$ is added to simulate shot noise. The optical wave begins with no modulation but undergoes substantial gain during the first 100 passes. The bottom left window plots the gain per pass. By $n \approx 50$, the optical wave is already displaying some modulation and by $n \approx 200$ the modulation is easily visible as the fluctuations in intensity across the middle-left window. The top-left window shows the final power at the end of the 1000th pass which is clearly modulated. The modulation is caused by the electrons which slip back past the optical field sites and execute synchrotron oscillations. The synchrotron frequency is imposed on the optical wave over many passes, so that only a small fraction of a synchrotron oscillation is sufficient to pass information to the optical wave. The bottom-right window plots the total average power in the oscillator. Note the power saturates at $n \approx 100$, but begins to grow slowly at $n \approx 250$ as the modulations in the main

49
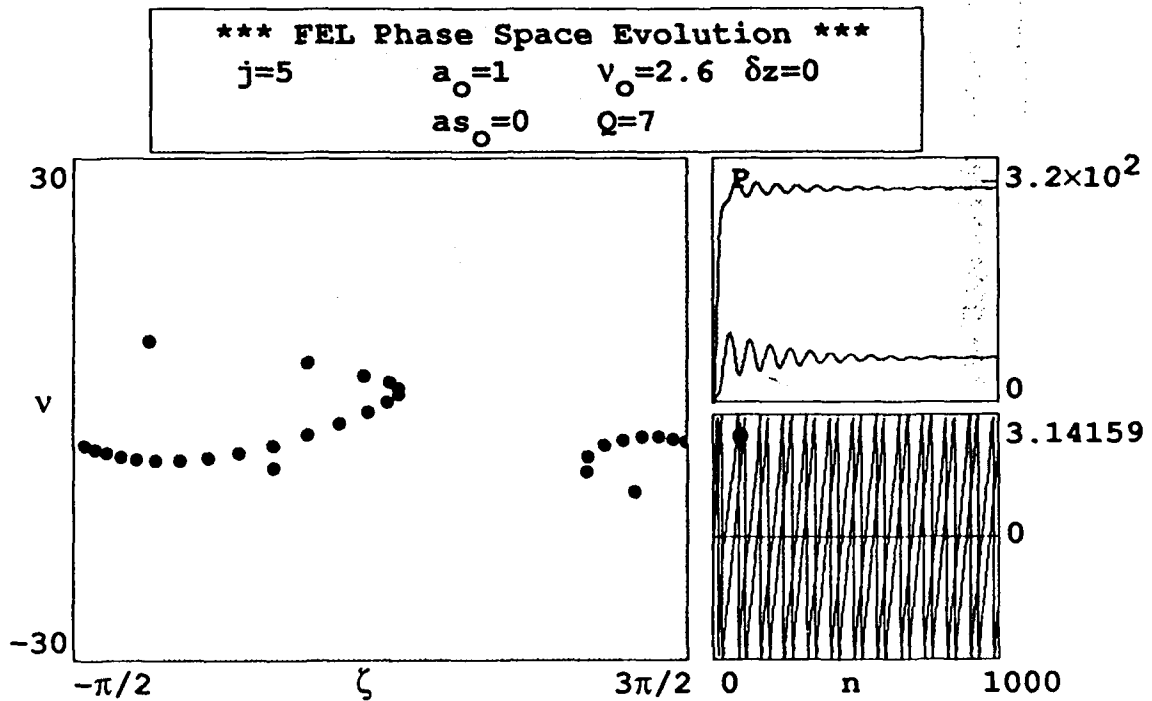
Figure 4-3: Two-mode simulation with j = 5, Q = 7, for comparison with figure 4-4.

lobe become more pronounced from the growing sideband. The sideband and the main lobe are clearly visible in the middle-center window where the power versus frequency is plotted with the same gray scale at the end of each pass. The main lobe is clearly visible as the thick, white line down the center of the window with the sideband approximately 2π away becoming visible at about $n \approx 250$. The top-center window is a plot of the final power versus frequency. The ratio of power between the sideband and the main lobe is about 1/5 which compares favorably with the two-mode simulation of Figure 4-3. The right-middle window is a plot of electron phase-velocity at the end of each pass. It is interesting to note the phase velocities spread out as the sideband becomes more pronounced. The top-right window plots the final electron phase-velocity distribution. The bottom center window is a plot of the gain spectrum. In the multi-mode simulation, the total final power is 3.2×10^2 which compares favorably with the total power of 3.2×10^2 in the two-mode simulation.
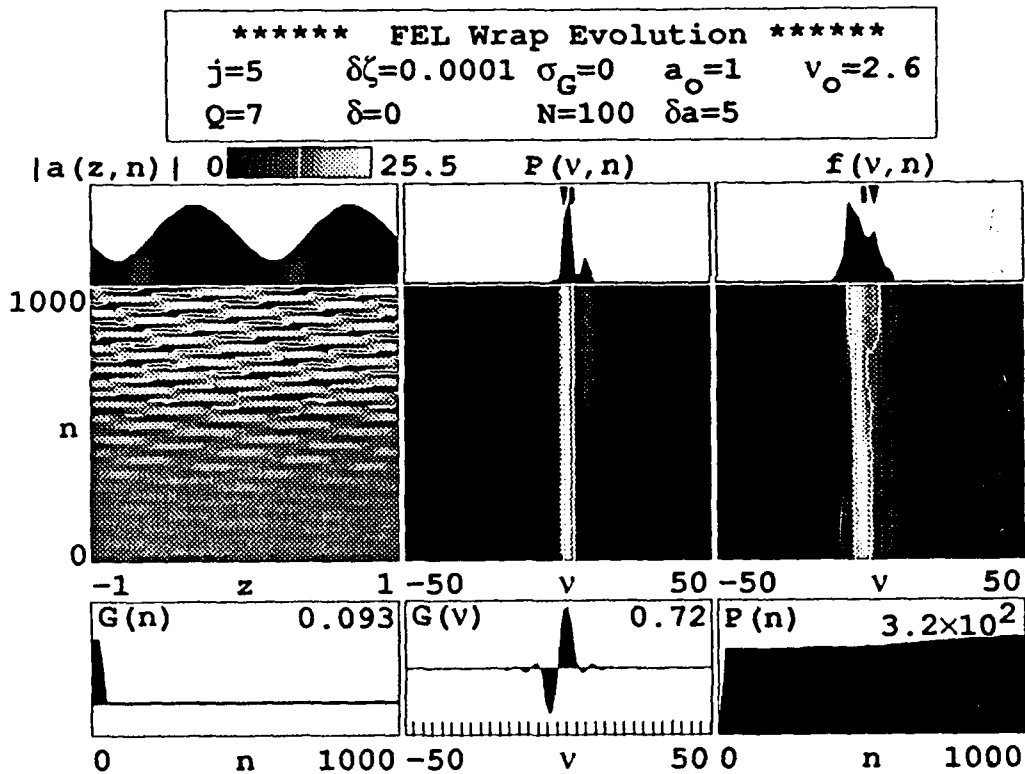
Figure 4-4: Multi-mode simulation with j = 5, Q = 7, showing the onset of a single sideband.

Figure 4-5 and Figure 4-6 show a two-mode and multi-mode simulation similar to the examples above, but now $Q = 9$. The higher Q value allows the sideband to fully develop to a power comparable to the main lobe. In Figure 4-5, the two-mode simulation shows the sideband being fully developed at $n = 390$. Before becoming fully developed, the sideband undergoes two large fluctuations before reaching the power of the main lobe and stabilizing. These fluctuations will be examined in more detail in the next subsection. The multi-mode simulation shows the sideband developing much sooner, and being completely developed by $n \approx 170$ without the large fluctuations of the two-mode model. In the multi-mode simulation, single-mode saturation occurs at $n \approx 50$, but growth of the total power continues as the sideband grows from $n \approx 50$ to $n \approx 170$. A second sideband begins to appear at $n \approx 180$, but never grows to a comparable power. The two-mode simulation has a total power of $P = 4.4 \times 10^2$ which compares well with $P = 5.9 \times 10^2$ for the multi-

51

*** FEL Phase Space Evolution ***
j=5 a_o=1 v_o=2.6 δz=0
as_o=0   Q=9
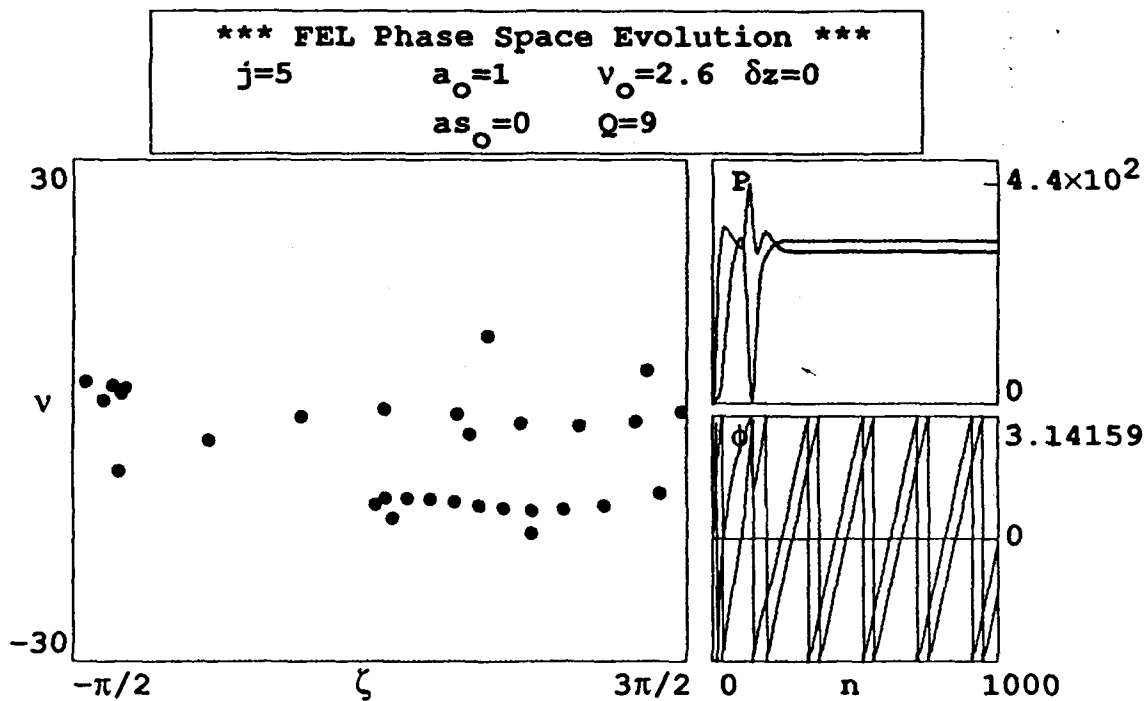
Figure 4-5: Two-mode simulation showing sideband growth that is comparable to the main lobe.

mode simulation. In the multi-mode simulation, the optical power is strongly modulated from the very beginning of the simulation because of the early growth of the sideband.

The last four examples were not to show that the simple two-mode model could get the same answer as the much more complicated multi-mode simulation, but were to show that the simple two-mode model is basically correct and produces results that can give insight into the development of sidebands. In the next subsection, the two-mode model produces results that give insight into an instability that leads to the onset of sidebands. Comparisons with the multi-mode simulation show that the instability is real and not an artificial feature of the two-mode model. It will be the simplicity of the two-mode model that will hopefully allow greater insight into the dynamics of the instability at the onset of sidebands.
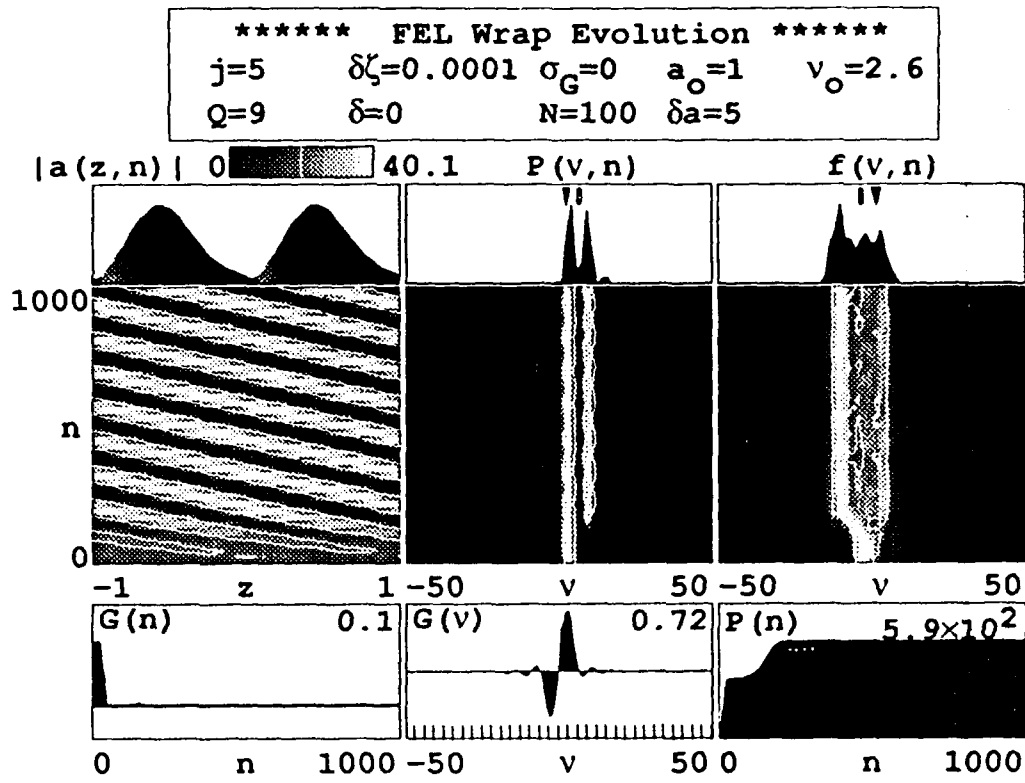
Figure 4-6: Multi-mode simulation with early growth of the sideband to powers comparable to the main lobe.

2. The Onset of Sidebands

Figures 4-7 through 4-12 illustrate a very interesting phenomena during the development of a sideband as Q is increased gradually over different simulations while holding $j = 5$ constant. In Figure 4-7, where $Q = 5$, the sideband only grows to about 1/5 of the power of the main lobe. Both the main mode and the sideband saturate very early at $n \approx 50$, and the sideband has a small "ripple" that quickly decays away. The main lobe achieved a power of $P = 2.0 \times 10^2$. In Figure 4-8, $Q = 6$, and the power in the main lobe is slightly higher at $P = 2.5 \times 10^2$, but the sideband is still about 1/5 of the power of the main lobe. The "ripple" in the sideband decays slower than in Figure 4-7 and the main lobe is beginning to pick up a similar "ripple". The optical phase changes rapidly. The "ripple" is now very pronounce in both the main lobe and the sideband. In Figure 4-9, $Q = 7.47$, the "ripple" no longer appears to decay. In Figure 4-10, $Q = 7.5$, the "ripple" is a growing oscillation. The mean power of the sideband is still about 1/5 of the mean power of the
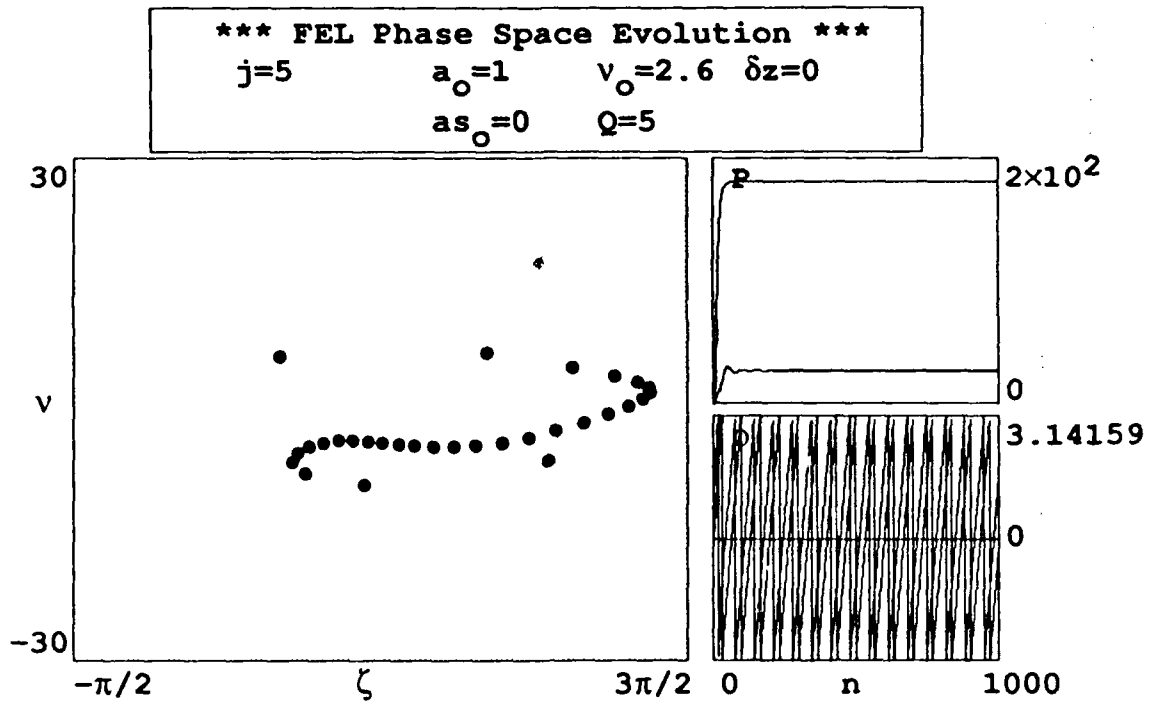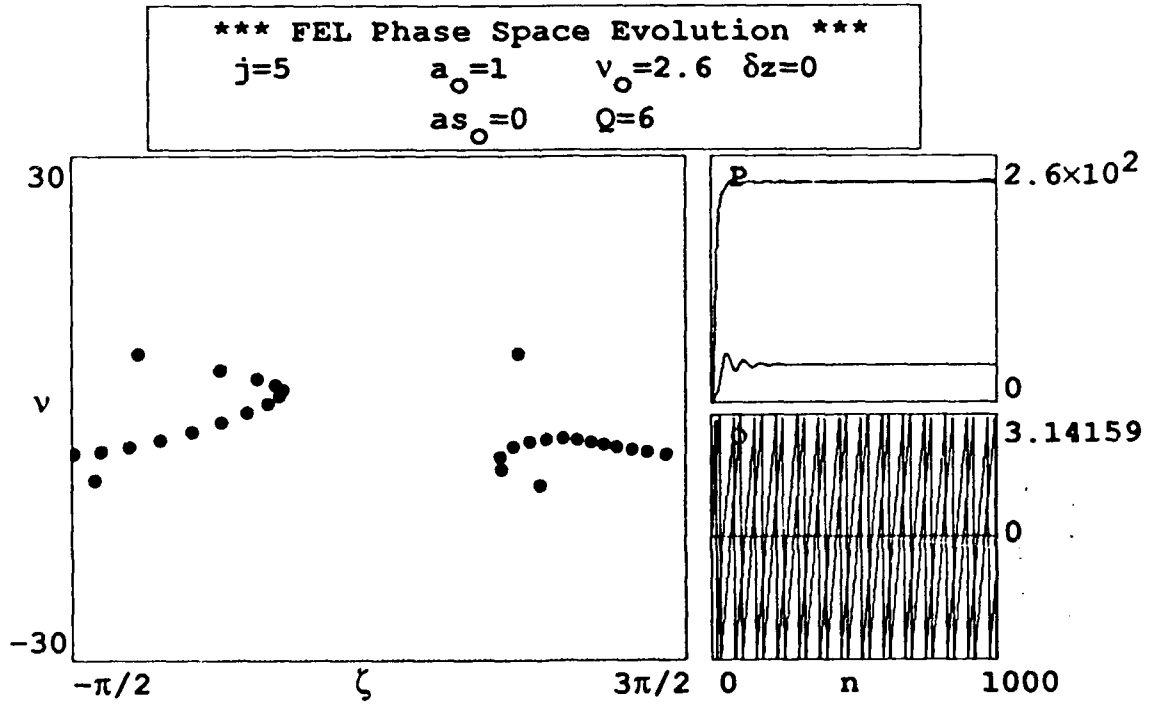
Figure 4-7: Onset of the sideband, j = 5, Q = 5.

Figure 4-8: Onset of the sideband, j = 5, Q = 6.

54

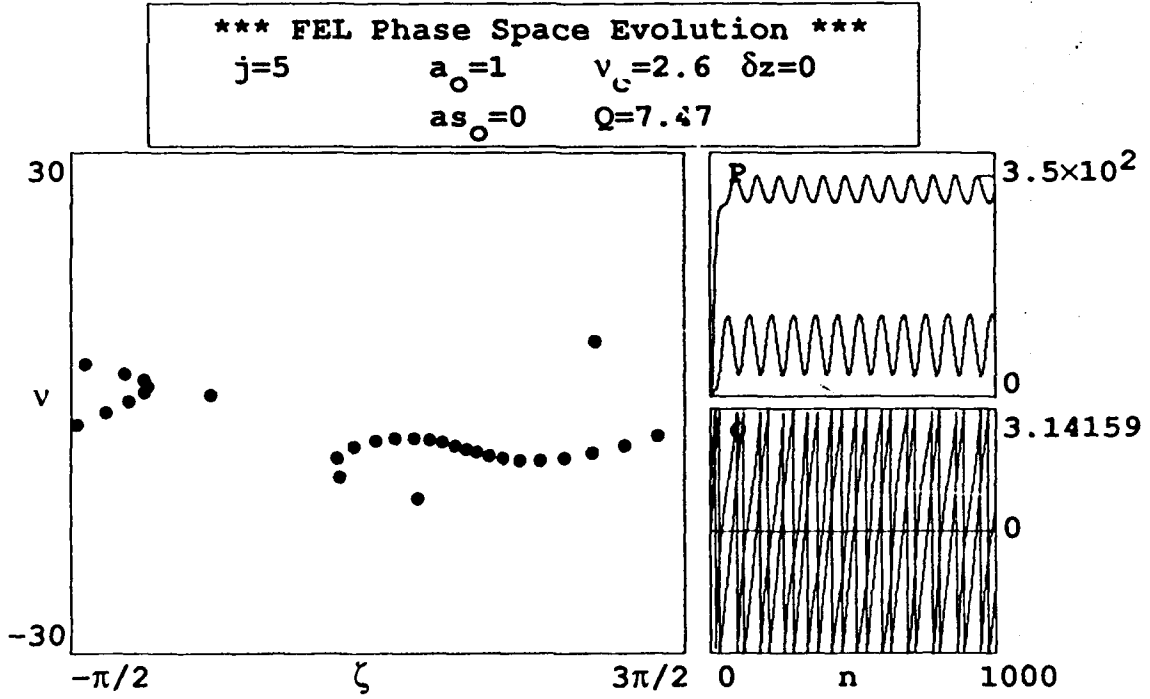Figure 4-9: Onset of the sideband, j = 5, Q = 7.47.

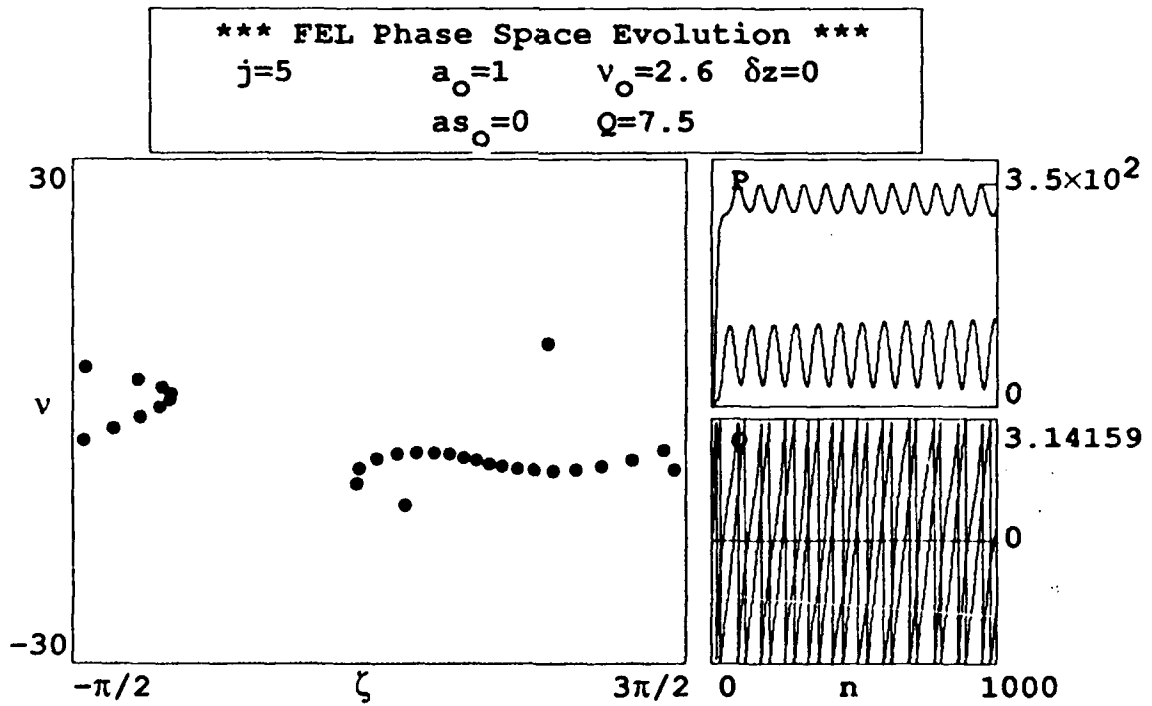Figure 4-10: Onset of the sideband, j = 5, Q = 7.5.

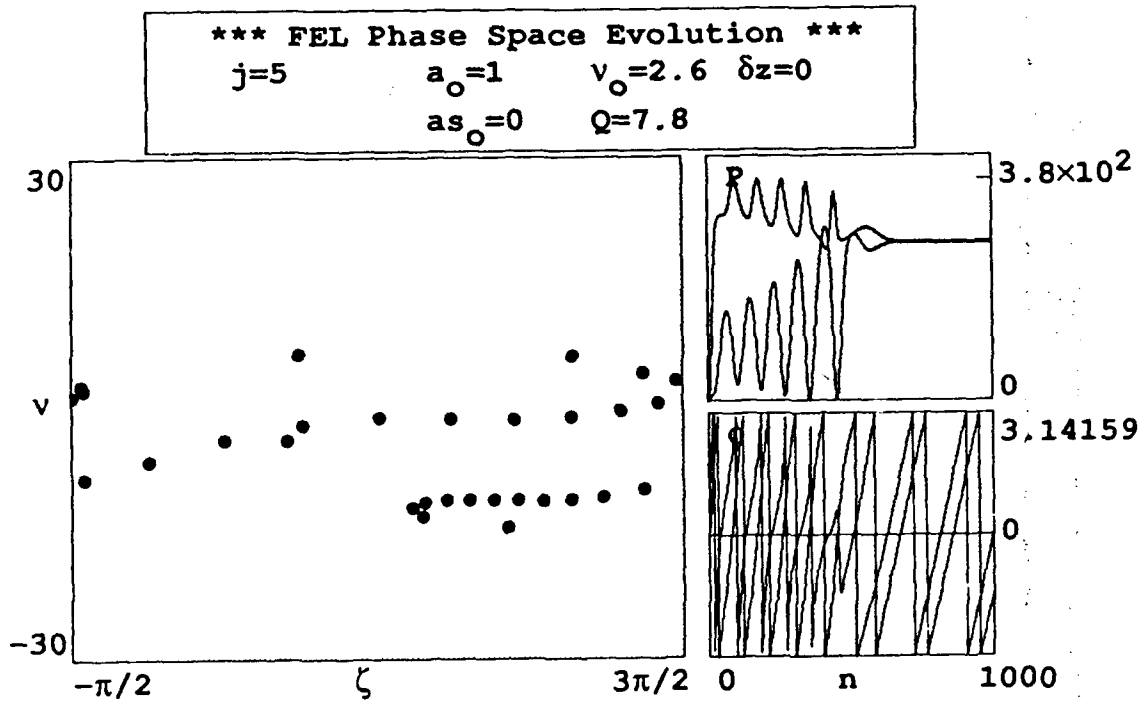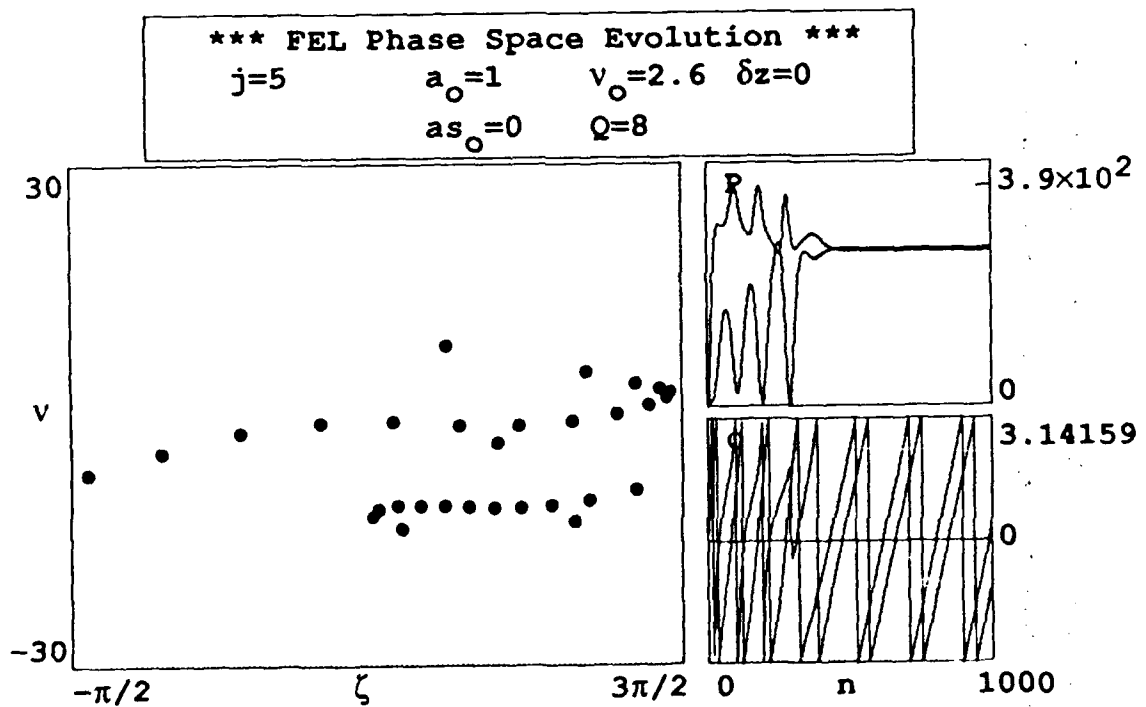***** FEL Phase Space Evolution *****

$j=5$ $a_o=1$ $v_o=2.6$ $\delta z=0$

$as_o=0$ $Q=7.8$

Figure 11: Onset of the sideband, $j = 5$, $Q = 7.8$.

*** FEL Phase Space Evolution ***

$j=5$ $a_o=1$ $v_o=2.6$ $\delta z=0$

$as_o=0$ $Q=8$

Figure 12: Onset of the sideband, $j = 5$, $Q = 8$.

main lobe. In Figure 4-11, $Q = 7.8$, several interesting changes happen in the simulation. First, the sideband's average power grows and the oscillations in the sideband's power evolution cross the main lobes's power evolution twice. Second, the main lobe's average power falls. Third, the sideband's power evolution, after crossing the main lobe's power evolution twice, oscillates to zero, then builds up to a steady power at nearly the same power as the main lobe. Fourth, in all the earlier simulations, the electrons were contained within a 2π region of phase-space so that $\Delta\zeta \leq 2\pi$, and only had to cross the periodic boundaries of phase-space once. In Figure 4-11, $\Delta\zeta \approx 3\pi$ since the electrons are widely spread in phase-space. Finally, note the difference in the optical phase evolution. In the previous examples, the optical phase of the sideband and the main lobe evolved rapidly, but at a constant rate and together. In Figure 4-11, the optical phase evolves much slower after the sideband reaches steady state. In Figure 4-12, $Q = 8$, the sideband's power evolution crosses the main lobe's power evolution twice before it reaches a steady state. Again, the optical phase evolution is slower after the sideband reaches steady state, and the electrons have a large spread, $\delta\zeta \leq 3\pi$.

The oscillations and instability presented in Figures 4-7 through 4-12 are not due to numerical integration errors. Numerous simulations were tried with many more particles and time steps and the oscillations still appeared with the same shape and frequency and only slightly different amplitude. Near the critical Q value that causes the "ripple" to start growing instead of decaying, the number of particles and time steps do affect the pass that sideband develops at. The "ripple" still has the same frequency. The slight differences between the simulations with more time steps and particles are most likely due to numerical accuracy. Figures 4-13 and 4-14 show simulations with 200 particles and 201 time steps to compare with Figures 4-3 and 4-11 which were run with 30 particles and 30 time steps.

The sequence of two-mode simulations in Figures 4-7 through 4-12 can be compared with multi-mode simulations at critical values of Q to show that certain key features exist between the two models. Some care must be exercised when making direct comparisons between the two-mode and
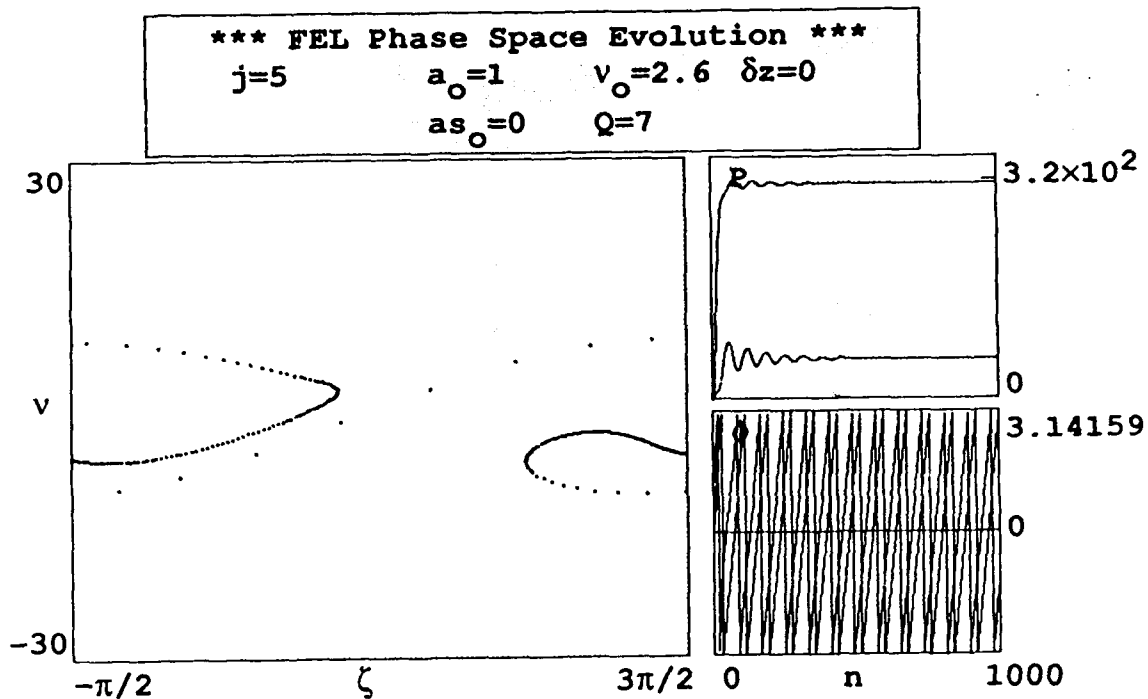
Figure 4-13: A simulation of 200 particles and 201 time steps at Q = 7.

multi-mode model since the two-mode model does not demonstrate much sensitivity to noise. Noise, however, has a strong influence on when the sidebands begin to develop in the multi-mode model and sidebands will not develop without some noise present in the multi-mode simulations. Figures 4-4 and 4-6 of the previous subsection are far enough away from the critical values of j and Q near the instability, that the noise sensitivity does not appear to affect the results substantially and the multi-mode model accurately reproduces comparable sideband power predicted by the two-mode model.

In Figure 4-15, the multi-mode simulation is run with $j = 5$, and $Q = 7.5$. The simulation also has a large amount of shot noise, $\delta\zeta = 0.001$ which tends to cause the sideband to develop early. This region of j and Q is similar to Figure 4-10, so that the sideband would now have a growing oscillation. Since the multi-mode simulation is run to 5000 passes, there is probably time
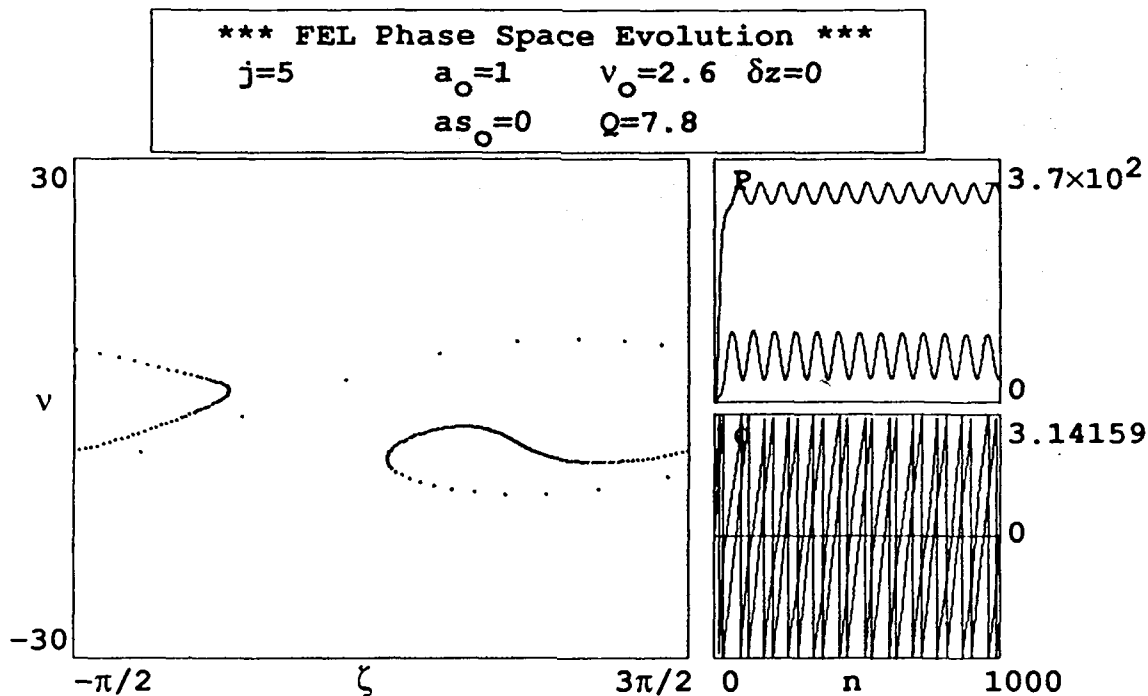
Figure 4-14: A simulation with 200 particles and 201 time steps at Q = 7.8.

for the sideband's power evolution to grow and overlap with the main lobe's power oscillation as happens dramatically in Figure 4-11. The large shot noise probably made this interaction happen at an earlier time than in the two-mode simulation. This overlapping of the side and main lobe power evolutions could be the cause of the sideband that appears to "grow" out of the main lobe in the center middle window of Figure 4-15 and then "grow" back into the main lobe. This process could repeat itself many times as the sideband and main lobe's oscillations slowly grow and merge as in the two mode model. It is also interesting to note that the electron phase velocities became more dispersed upon the first appearance of the sideband oscillation in Figure 4-15. This phenomenon also was apparent in the two-mode model. Note that the total power plot in the bottom right of Figure 4-15 is constant after the first 1000 passes implying that the main lobe and the side lobe are exchanging power as the merge and re-emerge with each other. This will produce the out of phase

```
******  FEL Wrap Evolution  ******
j=5      δζ=0.001   σ_G=0   a_o=1   v_o=2.6
Q=7.5    δ=0              N=100   δa=1
```
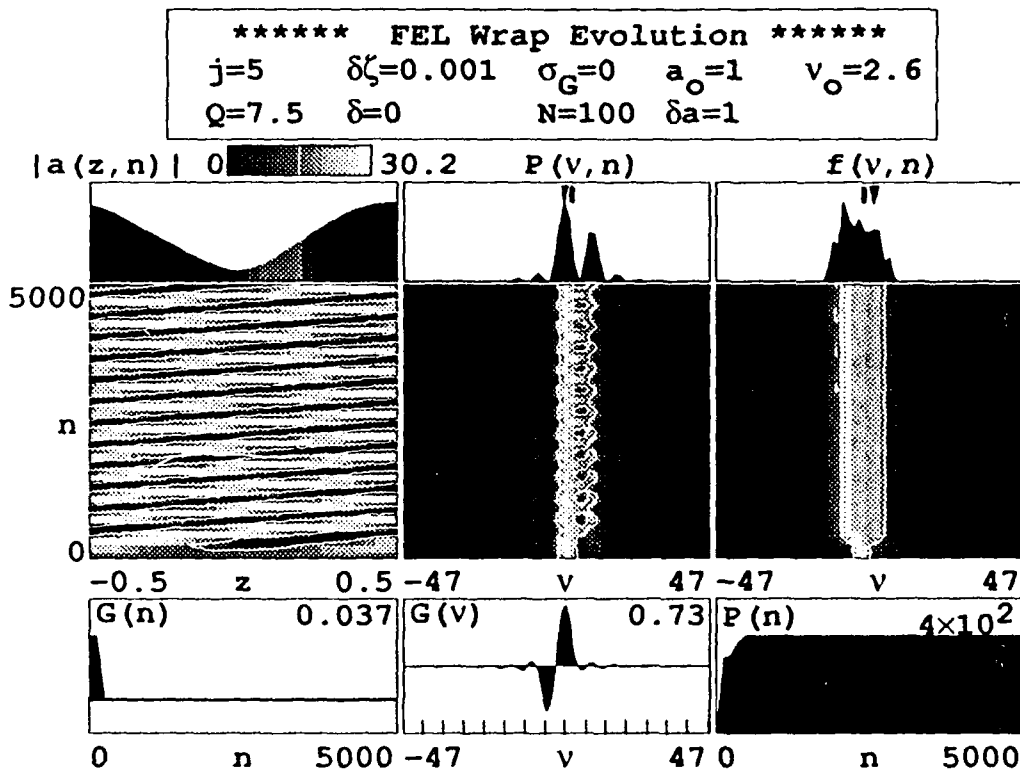
Figure 4-15: The emergence of a sideband out of the main lobe.

oscillations that are visible in the two-mode simulation of Figure 4-10.

Figure 4-16 is a multi-mode simulation with $j = 5$ and $Q = 7.6$ with no shot noise, but a large random fluctuations in the initial optical power, $\delta a = 5$. Here, the sideband starts growing almost immediately which is visible by the slight grey trail that forms early just to the right of the main lobe in the center-middle picture of Figure 4-16. However, it is not until $n \approx 280$ that the electron phase velocity widens substantially which is when the sideband is at nearly half the maximum power of the main lobe. The main lobe and sideband never merge in this simulation, but they both have oscillations across different frequencies as they evolve. Note that the total power does not become constant until $n \approx 400$.

The final three figures of this chapter demonstrate the simple oscillator model of section B.4 with the two-mode model. In these examples, $jQ = 39$ and $n/Q = 128.20513$ and are constants.
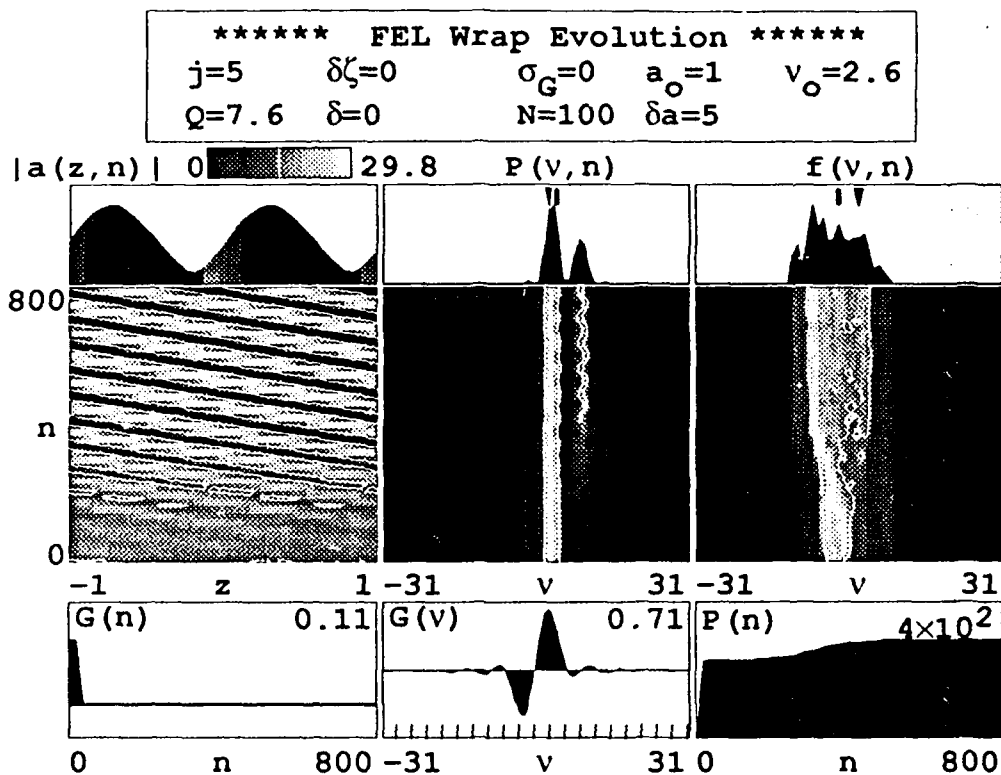
```
******  FEL Wrap Evolution  ******
j=5       δζ=0          σ_G=0    a_o=1    v_o=2.6
Q=7.6     δ=0           N=100    δa=5
```

Figure 4-16: Multi-mode simulation with the sideband developing early.

In Figure 4-17, $j = 2$, $n = 2500$ and $Q = 19.5$. In Figure 4-18, $j = 1$, $n = 5000$, and $Q = 39$. In Figure 4-19, $j = 0.5$, $n = 10000$, and $Q = 78$. Note all three simulations are similar, and the differences are probably due to numerical error. These figures also are similar to Figure 4-11 where, $j = 5$, $n = 1000$, and $Q = 7.8$.

D. CONCLUSION

Even though no quantitative theories for the development of sidebands in the FEL oscillator have been developed from the two-mode model, the two-mode model was instrumental in the discovery of the apparent instability that exists just prior to the growth of the first sideband. Together with the multi-mode model, the two-mode model will provide a powerful tool for the exploration of sideband development. It is the simplicity of the two-mode model that will probably provide the necessary intuitive understanding of the dynamics of sideband development to allow a simple,
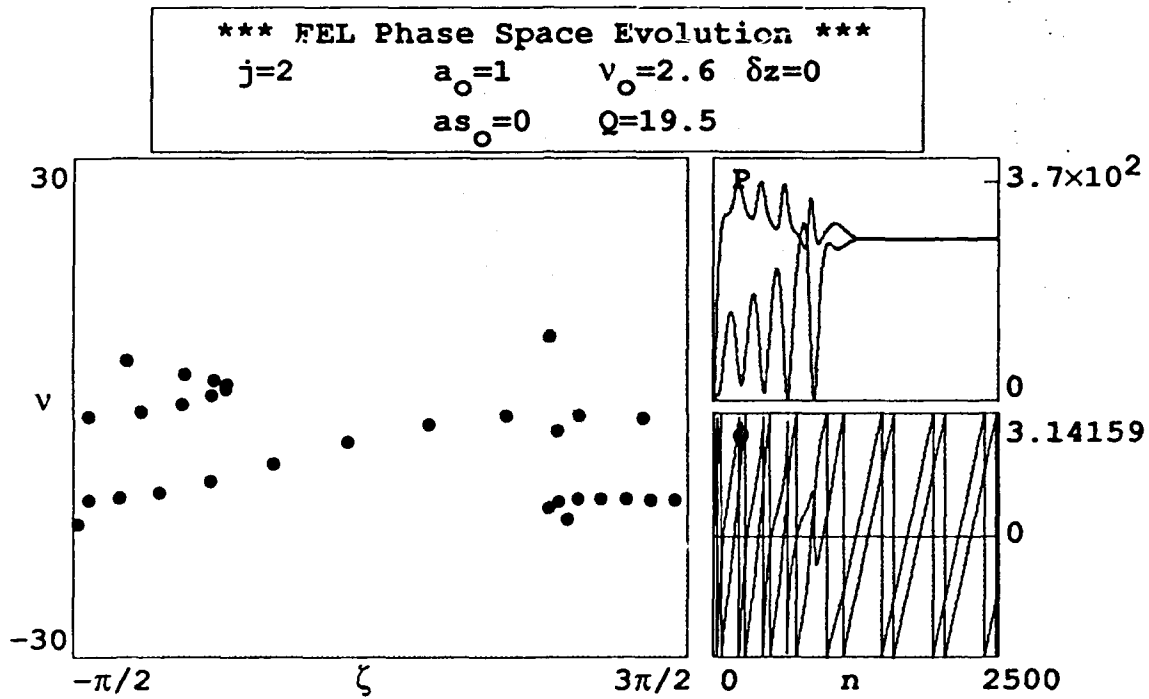
Figure 4-17; Simple oscillator comparisons, j = 2, Q = 19.5 and n = 2500.

quantitative theory to be developed explaining sideband development. The two-mode model can be easily extended to three or more modes without excessive loss of simplicity so that studies can be conducted on the onset of chaos as well as the growth of many sidebands.
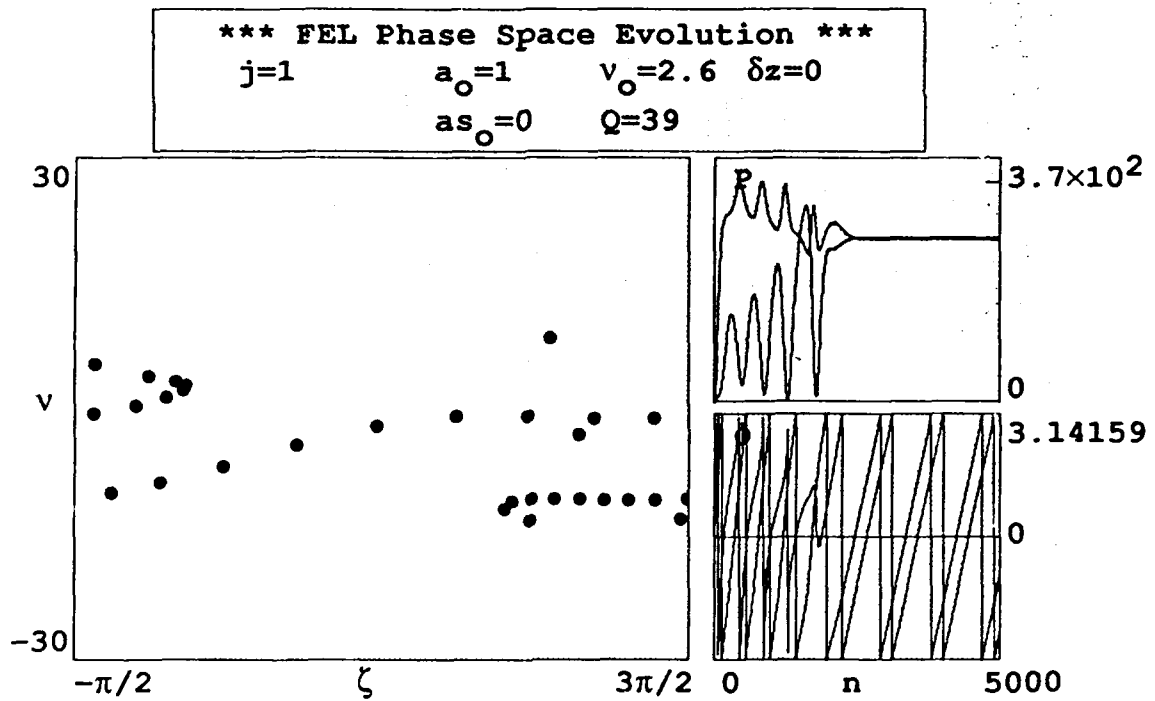
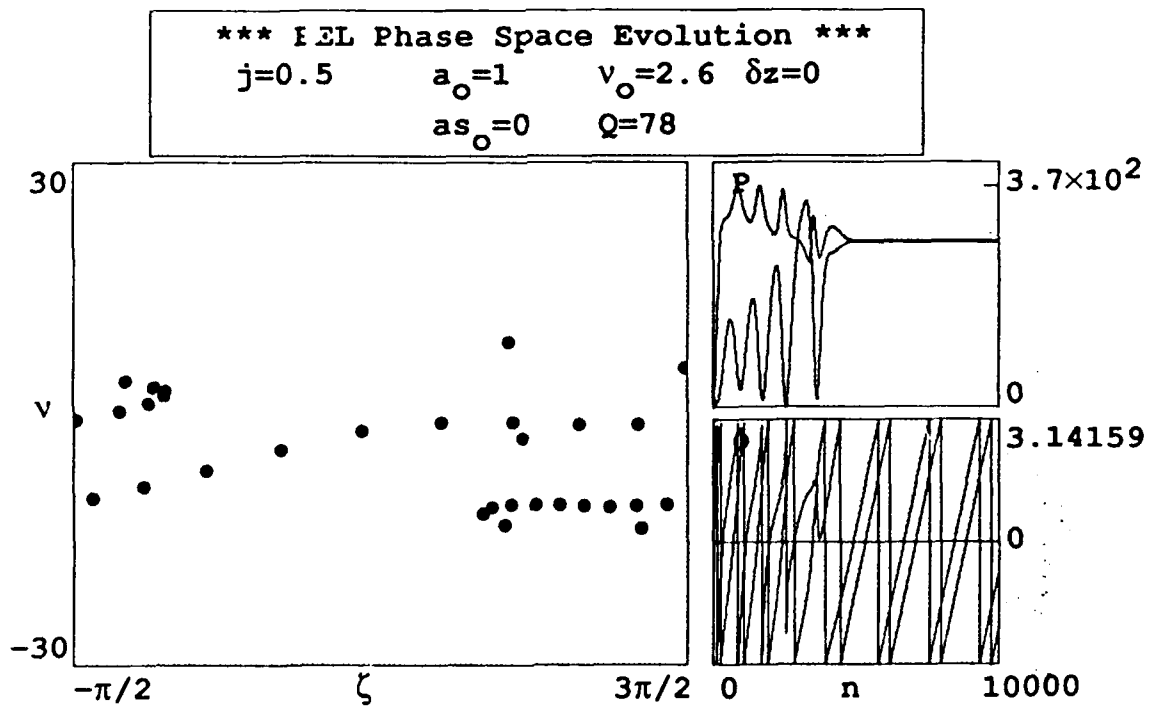Figure 4-18: Comparison of simple oscillator model, j = 1, Q = 39, n = 5000.

Figure 4-19: Comparison of simple oscillator model, j = 0.5, Q = 78, n = 10000.

63

LIST OF REFERENCES

[1] J. M. J. Madey, J. Appl. Phys. **42**, 1906 (1971).

[2] L. R. Elias, W. M. Fairbank, J. M. J. Madey, H. A. Schwettman, T. I. Smith, Phys. Rev. Lett. **36**, 717 (1976).

[3] D. A. G. Deacon, L. R. Elias, J. M. J. Madey, G. J. Ramian, H. A. Schwettman and T. I. Smith, Phys. Rev. Lett. **38**, 892 (1977).

[4] H. Motz and M. Nakamura, Ann. of Phys. **7**, 84 (1959).

[5] H. Motz, J. Appl. Phys. **22**, 527 (1951).

[6] H. Motz, W. Thon, R. N. Whitehurst, J. Appl. Phys. **24**, 826 (1953).

[7] R. M. Phillips, I. R. E. Trans. Electron Devices, 7, 231 (1960).

[8] W. B. Colson, *"Free Electron Laser Handbook"*, edited by W. B. Colson, C. Pellegrini and A. Reiieri (North-Holland Physics, Elsevier Science Publishing Co. Inc., The Netherlands, 1990), Chap. 5.

[9] J. Jackson, *"Classical Electrodynamics"*, (John Wiley and Sons, Inc., New York, 1975) pg. 222.

[10] N. M. Kroll, P. L. Morton, and M. N. Rosenbluth, in *Free Electron Generators of Coherent Radiation*, edited by S. F. Jacobs, H. S. Pilloff, M. S. Sargent III, M. O. Scully, and R. Spitzer (Addison-Wesley, Reading, Mass., 1980), p. 89.

[11] D. Prosnitz, A. Szoke, and V. K. Neil, Phys. Rev. **A 24**, 1436

(1981).

[12] K. Takayama, Phys. Rev. Lett. **63**, 516 (1989).

[13] R. Bonifacio, F. Casagrande and L. A. Lugiato, Optics Comm. **36**, (1981).

[14] T. J. Orzechowski, B. R. Anderson, J. C. Clark, W. M. Fawley, A. C Paul, D. Proznitz, E. T. Scharlemann, S. M. Yarema, A. M. Sessler, D. B. Hopkins, and J. S. Wurtele, Phys. Rev. Lett. **57**, 2172 (1986).

[15] T. H. Orzechowski, B. R. Anderson, W. M. Fawley, D. Prosnitz, E. T. Scharlemann, S. M. Yarema, A. M. Sessler, D. B. Hopkins, A. C. Paul and J. S. Wurtele, Nucl. Instr. and Meth. in Phys Res. **A250**, 144 (1986).

[16] W. B. Colson and R. A. Freedman, Optics Comm. **46**, 37 (1983).

[17] R. A. Freedman and W. B. Colson, Optics Comm. **52**, 409 (1985).

[18] W. B. Colson, *Free Electron Generators of Coherent Radiation*, SPIE **453**, 289, edited by Brau, Jacobs, and Scully (1984).

[19] D. C. Quimby, J. M. Slater, and J. P. Wilcoxon, IEEE Journal of Quantum Electronics, **QE-21**, 979 (1985).

[20] N. Kroll and M. N. Rosenbluth, *Physics of Quantum Electronics*, Vol. **7**, 147, (1980).

[21] W. B. Colson, Nucl. Instr. and Methods in Phys. Res., **A250**, 168 (1986).

INITIAL DISTRIBUTION LIST

1. Defense Technical information Center   2
    Cameron Station
    Alexandria, Virginia 22304-6145

2. Library, Code 52   2
    Naval Postgraduate School
    Monterey, California 93943-5002

3. Professor William B. Colson Code PH/CW   5
    Department of Physics
    Naval Postgraduate School
    Monterey, California 93943-5000

4. Professor K. E. Woehler Code PH/WH   1
    Department of Physics
    Naval Postgraduate School
    Monterey, California 93943-5000